J. Fluid Mech. (2001), *vol.* 439, *pp.* 131–163. Printed in the United Kingdom

An experimental study of the dissipative and vortical motion in turbulent boundary layers

By YIANNIS ANDREOPOULOS AND ANANT HONKAN†

Experimental Fluid Mechanics and Aerodynamics Laboratory, Department of Mechanical Engineering, The City College of the City University of New York, Convent Avenue and 140th Street, New York, NY 10031, USA

(Received 27 January 2000 and in revised form 13 November 2000)

The experimental data of Honkan & Andreopoulos (1997*a*) have been further analysed and some new statistical results obtained. In the present work, particular emphasis is given to the time-dependent behaviour of the kinematic shear stress, vorticity, enstrophy, dissipation rate, vorticity stretching and several of the matrix invariants of the velocity-gradient tensor, strain-rate tensor and rotation-rate tensor. The invariants are linked with terms appearing in the transport equations of enstrophy and dissipation rate. Indicative of the existence of extremely high fluctuations is that all r.m.s. values are considerably larger than the corresponding mean values. All invariants exhibit a very strong intermittent behaviour, which is characterized by large amplitude of bursts, which may be of the order of 10 times the r.m.s. values. A substantial qualitative agreement is found between the present experimentally obtained statistical properties of the invariants and those obtained from direct numerical simulation data. Patterns with high rates of turbulent kinetic energy dissipation and high enstrophy suggest the existence of strong shear layers in the near-wall region. In many instances, locally high values of the invariants are also associated with peaks in the shear stress. Conditional analysis provides some evidence of the existence of sequences of several vortices during strong vortical activities, with an average frequency of appearance four times higher than the frequency of appearance of hairpin vortices.

1. Introduction

Turbulence is characterized by a large variety of scales. Large scales are responsible for the bulk transport of momentum or heat while small scales contribute significantly in carrying out mixing at the molecular level. The role of small scales in the overall behaviour of turbulence is not well understood. It is known, for instance, that small scales transport heat more efficiently than momentum while large scales transport momentum more efficiently than heat (see Chevray & Tutu 1978). It is also known that small scales carry a significant amount of vorticity and contribute substantially to the dissipation rate of turbulent kinetic energy. In addition, large-eddy simulation (LES) methods, which are growing in number and range of applications that include complex geometries, require information about small scales for modelling the subgrid scales. In LES the dynamics of the fine-scale motions cannot be captured and therefore need to be modelled.

There is considerable interest in studying the dissipative motions of turbulent flows particularly in wall-bounded flows. In the present experimental work, the dissipative

† Present address: Georgia Perimeter College, Clarkston, GA30021, USA.

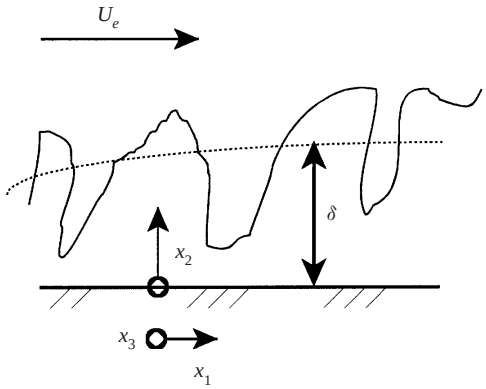

FIGURE 1. Boundary layer flow schematic and coordinates.

motions in a two-dimensional turbulent boundary layer have been investigated by carrying out measurements of the complete velocity gradient tensor $\partial U_i/\partial x_j$ using instrumentation with high temporal and spatial resolution (see figure 1 for a schematic of the flow and the definition of the coordinate system). Information on the velocity gradient tensor can lead to additional information on the rate-of-strain tensor S_{ij}, the rate-of-rotation tensor R_{ij} and the rate of dissipation of turbulent kinetic energy ε which can help in a better understanding of these complicated turbulent motions. One way to provide information on this is to study the topology of these motions by looking at the behaviour of the matrix invariants of all the tensors mentioned above. Soria *et al.* (1994) and Cantwell (1993) studied the fine-scale turbulent motions of plane mixing layers by considering all the matrix invariants of the velocity gradient tensor, the rate-of-strain tensor and the rate-of-rotation tensor. The data generated in the direct numerical simulation (DNS) of Moser & Rogers (1993) and used in their studies indicated that the rate-of-strain tensor topology is characterized as an unstable node–saddle–saddle configuration. Topological features of the fine-scale motions in turbulent boundary layers and channel flows have been investigated by Chaćin, Cantwell & Kline (1996) and by Blackburn, Mansour & Cantwell (1996), respectively. DNS data from Spalart (1988) and Kim, Moin & Moser (1987) were analysed in these investigations.

Thus far, the importance of the matrix invariants of these tensors as tools in turbulence research has been demonstrated through theoretical analysis of DNS data. The objective of the present work is to consider the issues related to matrix invariants by analysing existing data obtained experimentally in a zero-pressure-gradient turbulent boundary layer and documented in Honkan & Andreopoulos (1997*a*), hereafter referred to as HA. Experimentally obtained measurements of the rate-of-strain, the rate-of-rotation and the velocity gradient tensors have only recently become available (Tsinober, Kit & Dracos 1992; Balint, Wallace & Vukoslavcevic 1991; Honkan & Andreopoulos 1997*a*). Time-dependent measurement of all the elements of these tensors is a formidable task. The difficulties associated with the measurements of velocity gradients are described in the recent review article of Wallace & Foss (1995). Issues related to spatial and temporal resolution appear to be the most significant among all that were considered.

An additional objective of the present study is to identify any differences that may exist between computational and experimental data obtained by analysis of matrix invariants. One likely difference may be due to the fact that most of the computational

results and analysis of matrix invariants have been based on inviscid theory (see Cantwell 1993) even though DNS data have been used for their verification. In plane mixing layers, for instance, the effects of viscosity on flow topology may not be very significant. In wall-bounded flows, however, the viscous layer above the wall may have a significant effect on the local flow topology.

The availability of reliable experimental data of these tensors led to some further analysis, which helped to better understand the behaviour of turbulent motions in wall-bounded flows. In particular, the role of the instantaneous shear stress u_1u_2 in dynamically significant events is further explored because the conditional sampling work presented in HA has indicated that highly dissipative motions as well as highly vortical motions are associated with the presence of substantial values of u_1u_2.

A multi-sensor hot-wire probe has been developed, tested, and applied in various flows. The probe is capable of measuring the time-dependent rate-of-strain tensor, the rate-of-rotation tensor i.e. vorticity vector, and the rate of dissipation of turbulent kinetic energy with adequate spatial resolution. The statistical averages obtained in a two-dimensional boundary layer have been successfully compared to a variety of available DNS and experimental data. The reader is referred to HA for an extensive description of the experimental techniques used and assessment of the performance of the probe. Measurements of velocity gradients tensors with this probe have been extended to vortex-dominated flows (Honkan & Andreopoulos 1997*b*), mildly compressible grid turbulence (see Briassulis, Agui & Andreopoulos 2001) and turbulence or vortex interactions with shock waves (see Andreopoulos, Agui & Briassulis 2000).

Section 2 of the present work provides a brief analysis of the local flow topology theory while the transport equations of the tensors are discussed in § 3. A short description of the experimental set-up, instrumentation and techniques used is given in § 4. The results are presented in § 5, vortex streaks are discussed in § 6, and the conclusions are summarized in § 7.

2. Local flow topology

For an observer travelling with the local velocity at a given point inside a flow, the geometry of the instantaneous flow pattern at some point in the neighbourhood can be described, to first order, using the terminology of the critical point theory of Perry & Chong (1987) and Chong, Perry & Cantwell (1990). According to this theory the local flow topology can be classified according to the nature of the eigenvalues λ of the velocity gradient tensor $A_{ij} = \partial U_i/\partial x_j$ that are the roots of the cubic equation

$$\det [A_{ij} - \lambda\delta_{ij}] = \lambda^3 + P\lambda^2 + Q\lambda + R = 0, \tag{2.1}$$

where the coefficients P, Q and R are the invariants of the tensor since their values are unchanged by rotation of the coordinate frame. These invariants are

$$\begin{aligned} P &= -\text{trace}\,[\boldsymbol{A}] \\ Q &= \tfrac{1}{2}(P^2 - \text{trace}\,[\boldsymbol{A}^2]) \\ R &= -\det[\boldsymbol{A}] \end{aligned}$$

The velocity gradient tensor A_{ij} can be decomposed, non-uniquely, into a symmetric part, the rate-of-strain tensor

$$S_{ij} = \tfrac{1}{2}(\partial U_i/\partial x_j + \partial U_j/\partial x_i)$$

and the antisymmetric part, the rate-of-rotation tensor

$$R_{ij} = \tfrac{1}{2}(\partial U_i/\partial x_j - \partial U_j/\partial x_i) = \tfrac{1}{2}\varepsilon_{ijk}\Omega_k$$

where Ω_k is the vorticity vector and ε_{ijk} is the alternating unit tensor. Thus

$$\partial U_i/\partial x_j = A_{ij} = S_{ij} + R_{ij}$$

and consequently the invariants can be expressed in terms of S_{ij} and R_{ij} as

$$P = -S_{ii}, \tag{2.2}$$

which is zero for incompressible flows like the present one,

$$Q = \tfrac{1}{2}(-S_{ij}S_{ij} + R_{ij}R_{ij}) \tag{2.3}$$

and

$$R = -\tfrac{1}{3}(S_{ij}S_{jk}S_{ki} + 3R_{ij}R_{jk}S_{ki}) \tag{2.4}$$

The invariants of the rate-of-strain tensor S_{ij}, P_S, Q_S and R_S can be similarly generated by setting $R_{ij} = 0$ (see Soria *et al.* 1994) in the previous relations:

$$P_S = 0, \quad Q_S = -\tfrac{1}{2}S_{ij}S_{ij}, \quad R_S = -\tfrac{1}{3}S_{ij}S_{jk}S_{ki}.$$

One can also obtain the invariants of the rate-of-rotation tensor R_{ij}:

$$P_R = 0, \quad Q_R = \tfrac{1}{2}R_{ij}R_{ij}, \quad R_R = 0.$$

The various flow topologies that can occur in the plane $P = 0$, which corresponds to incompressible flows, are determined by the sign of the discriminant

$$D = \tfrac{27}{4}R^2 + Q^3. \tag{2.5}$$

If $D > 0$ then there are one real and two complex-conjugate solutions of the characteristic equation (2.1) which are called foci. If $D < 0$, equation (2.1) admits three real solutions, which are called node–saddle–saddle according the terminology introduced by Perry & Chong (1987).

It is important to notice that the topological classification at a given point of the flow will be independent of the frame of reference chosen since it depends on D, i.e. on R and Q, which are invariant to translation of the reference frame. As will be shown in the next section these invariants are also related to dynamically important quantities of the flow. It is apparent, for instance, that Q_S is proportional to the dissipation rate and that Q_R is related to the enstrophy density $(1/2)\Omega_i\Omega_i$.

3. Transport equations

The incompressible Navier–Stokes equations in tensor notation,

$$\frac{\mathrm{D}U_i}{\mathrm{D}t} = -\frac{1}{\rho}\frac{\partial P}{\partial x_i} + \frac{1}{\rho}\frac{\partial \tau_{ki}}{\partial x_k}, \tag{3.1}$$

give a coupled set of equations for the rate-of-rotation tensor R_{ij} and the rate-of-strain-tensor S_{ij} in a Lagrangian reference frame:

$$\frac{\mathrm{D}R_{ij}}{\mathrm{D}t} = S_{ik}R_{kj} - S_{jk}R_{ki} + \nu\frac{\partial^2 R_{ij}}{\partial x_k \partial x_k}, \tag{3.2}$$

$$\frac{\mathrm{D}S_{ij}}{\mathrm{D}t} = -S_{ik}S_{kj} - R_{ik}R_{kj} - \frac{1}{\rho}\frac{\partial^2 P}{\partial x_i \partial x_j} + \nu\frac{\partial^2 S_{ij}}{\partial x_k \partial x_k}, \tag{3.3}$$

$$\frac{1}{\rho}\frac{\partial^2 P}{\partial x_k \partial x_k} = R_{ik}R_{ik} - S_{ik}S_{ik}, \tag{3.4}$$

where $\mathrm{D}/\mathrm{D}t = \partial/\partial t + U_k \partial/\partial x_k$ is the total derivative, τ_{ki} is the shear stress, P is the instantaneous pressure, ρ is the density of fluid and ν is the kinematic viscosity. In the notation above, a capital letter indicates time-dependent, total quantities while a lower-case letter indicates the fluctuating part about the mean value, the latter being indicated with an overbar.

Equation (3.2) is better known as a vorticity transport equation if the substitution $R_{ij} = 1/2\varepsilon_{ijk}\Omega_k$ is made:

$$\frac{\mathrm{D}\Omega_i}{\mathrm{D}t} = S_{ik}\Omega_k + \nu\frac{\partial^2 \Omega_i}{\partial x_k \partial x_k} \tag{3.5}$$

The transport equation for the rate-of-rotation tensor describes several dynamically significant processes for the rotating eddies, namely stretching or compression of vorticity by strain and viscous diffusion down a vorticity gradient. The viscous term may also describe re-connection of vortex lines at very small scales due to viscosity. It should be noted that the terms expressing stretching or compressing of vortex lines or tubes also contain changes in vorticity due to re-orientation/rotation of vorticity by strain. In the present context, the use of the term stretching also includes the notion of re-orientation of the vorticity vector. The convection of vorticity has the characteristic that it is preserved on a particle path, which implies that the vorticity can only be transferred to the neighbouring fluid particle by diffusion, i.e. by the effect of viscosity. The diffusion, together with the convection, results in the spread/decay of vorticity and thus plays a vital role in the development of vortical flows. Unlike Navier–Stokes equations for momentum conservation, the pressure term does not appear explicitly in the vorticity transport equation and therefore enables simplification in the computation and interpretation of the theoretical models of more 'complex' flows.

The dynamical equation for the strain $\boldsymbol{S}$ is more complex. In addition to the nonlinear interaction and viscous smoothing, the strain undergoes rotation due to vorticity and is subject to the non-local action of the pressure hessian $\partial^2 P/(\partial x_i \partial x_j)$.

The above equations can be manipulated to obtain the transport equation for the enstrophy density $(1/2)\Omega_k\Omega_k = R_{ij}R_{ij}$:

$$\frac{\mathrm{D}(R_{ij}R_{ij})}{\mathrm{D}t} = 2S_{ik}R_{kj}R_{ij} + 2S_{jk}R_{ik}R_{ij} + \nu\frac{\partial^2 (R_{ij}R_{ij})}{\partial x_k \partial x_k} - 2\nu\left(\frac{\partial R_{ij}}{\partial x_k}\right)\left(\frac{\partial R_{ij}}{\partial x_k}\right). \tag{3.6}$$

The transport equation for the time-dependent quantity U_iU_j contains the dissipation tensor E_{ij}:

$$\frac{\mathrm{D}U_iU_j}{\mathrm{D}t} = -\frac{1}{\rho}U_j\frac{\partial P}{\partial x_i} - \frac{1}{\rho}U_i\frac{\partial P}{\partial x_j} + \frac{1}{\rho}\frac{\partial U_j\tau_{ki}}{\partial x_k} + \frac{1}{\rho}\frac{\partial U_i\tau_{kj}}{\partial x_k} - E_{ij}, \tag{3.7}$$

where

$$E_{ij} = \frac{1}{\rho}\tau_{ki}\frac{\partial U_j}{\partial x_k} + \frac{1}{\rho}\tau_{kj}\frac{\partial U_i}{\partial x_k}, \tag{3.8}$$

which is equivalent to

$$E_{ij} = 2\nu\left[S_{ik}\frac{\partial U_j}{\partial x_k} + S_{jk}\frac{\partial U_i}{\partial x_k}\right] = 2\nu[S_{ik}S_{jk} + S_{jk}S_{ik} + S_{ik}R_{jk} + S_{jk}R_{ik}]. \tag{3.9}$$

For the dissipation rate of the total kinetic energy $(1/2)U_iU_i$ the above relation becomes

$$E = \tfrac{1}{2}E_{ii} = 2\nu[S_{ik}S_{ik}]. \tag{3.10}$$

The transport equation (3.3) can be used to obtain the transport equation for $2S_{ij}S_{ij}$, which is proportional to the instantaneous E:

$$\begin{aligned}\frac{\mathrm{D}(2S_{ij}S_{ij})}{\mathrm{D}t} = &-4S_{ik}S_{kj}S_{ij} + 4R_{jk}R_{ki}S_{ij} \\ &-4S_{ij}\frac{1}{\rho}\frac{\partial^2 P}{\partial x_i \partial x_j} + \nu\frac{\partial^2(2S_{ij}S_{ij})}{\partial x_k \partial x_k} \\ &-4\nu\left(\frac{\partial S_{ij}}{\partial x_k}\right)\left(\frac{\partial S_{ij}}{\partial x_k}\right).\end{aligned} \tag{3.11}$$

If one considers the following relation for the time dependent turbulent kinetic energy $1/2u_iu_i$:

$$\tfrac{1}{2}u_iu_i = \tfrac{1}{2}U_iU_i - u_i\overline{U}_i - \tfrac{1}{2}\overline{U}_i\overline{U}_i, \tag{3.12}$$

then the transport equation for it could be rewritten as

$$\frac{\mathrm{D}\frac{1}{2}u_iu_i}{\mathrm{D}t} = -\frac{1}{\rho}\frac{\partial pu_i}{\partial x_i} + \frac{1}{\rho}\frac{\partial u_i[\tau_{ki} + \rho\overline{u_iu_k}]}{\partial x_k} - u_iu_k\frac{\partial \overline{U}_i}{\partial x_k} - \overline{u_iu_k}\frac{\partial u_i}{\partial x_k} - 2\nu s_{ij}s_{ij}, \tag{3.13}$$

and the source term with the meaning of production of turbulent kinetic energy could be rewritten as

$$P_u = -u_iu_k\frac{\partial \overline{U}_i}{\partial x_k} - \overline{u_iu_k}\frac{\partial u_i}{\partial x_k} = -u_iu_k\frac{\partial U_i}{\partial x_k} + (u_iu_k - \overline{u_iu_k})\frac{\partial u_i}{\partial x_k}, \tag{3.14}$$

where the last term inside the parentheses indicates the fluctuation of shear stress above its mean value. Equation (3.13) indicates that the time-dependent dissipation rate of the turbulent kinetic energy appears to be

$$\varepsilon = 2\nu[s_{ik}s_{ik}]. \tag{3.15}$$

It should be mentioned that $\overline{S_{ij}S_{ij}} = \overline{S_{ij}}\ \overline{S_{ij}} + \overline{s_{ij}s_{ij}}$. This relation indicates that the time-average total dissipation rate of the total kinetic energy is different from the dissipation rate of the time-average turbulent kinetic energy by $\overline{S_{ij}}\ \overline{S_{ij}}$ which, in the present non-homogenous flow, is non-zero and reaches large values very close to the wall. It should also be mentioned that the fluctuating part of the two dissipation rates $S_{ij}S_{ij}$ and $s_{ij}s_{ij}$ about their mean values are related through $(S_{ij}S_{ij} - \overline{S_{ij}S_{ij}}) = (s_{ij}s_{ij} - \overline{s_{ij}s_{ij}}) + 2s_{ij}\overline{S_{ij}}$. Thus the two fluctuating components are not identical.

Note also that on time-averaging these time-dependent transport equations the well-known transport equations for mean turbulent quantities can be obtained. The intent of the previous derivation was to formulate transport equations for instantaneous quantities so that transport and source terms can be distinguished and to avoid the erroneous consideration of instantaneous quantities obtained by simply 'un-averaging' the transport equations for mean turbulent quantities.

A comparison between the invariants and various terms appearing in some of the transport equations derived above suggests that the second invariant Q of the velocity gradient tensor is related to equation (3.4):

$$Q = \frac{1}{2}\frac{1}{\rho}\frac{\partial^2 P}{\partial x_k \partial x_k}. \tag{3.16}$$

U_e (m s^{-1})	δ (mm)	θ/δ^* (mm)	c_f	u_τ (m s^{-1})	Re_θ
3.2	140 17.5	13.6/17.5	0.0033	0.13	2790

TABLE 1. Principal flow parameters: U_e is the free-stream velocity, δ the boundary layer thickness, θ the momentum thickness, c_f the friction coefficient, u_τ the friction velocity and Re_θ, Reynolds number based on θ.

It is also obvious that $Q_S = -E/(4\nu)$ and $Q_R = (1/4)\Omega_k\Omega_k$. The first term of the third invariant R of equation (2.4) or the invariant R_S appear as a source term in (3.11) and the second term of R is a source term in (3.6). Thus the invariants can be used to obtain information on the transport equation of dynamically significant flow quantities.

It should be pointed out that the invariants are related to the instantaneous total quantities and not to the time-dependent turbulent part only.

4. Experimental set-up, instrumentation and techniques

The experimental investigations in this research have been carried out in the wind tunnel of The Mechanical Engineering Department, at CCNY. The tunnel is of open-ended suction type, with a 4 ft $\times$ 4 ft cross-section and has a 28 ft long working area. The motor and fan assembly is housed in a sound-absorbing diffuser allowing low noise operation of the facility and low levels of acoustical noise transmitted in the working section. It is also mounted on a frame which rests on eight springs to minimize vibration and isolates the motor and fan assembly from the working section. Three sides – top, bottom and one wall – of the working section are of 1 in. plywood while the other wall has four Plexiglas windows also of 1 in. thickness for observation. The inlet of the contraction section is fitted with honeycomb followed by three layers of fine steel screen to obtain uniform flow of turbulence intensity less than 0.1% for the maximum speed in the working section. This contraction section is 12 ft $\times$ 12 ft at one end, narrowing down to 4 ft $\times$ 4 ft, resulting in a 9 : 1 contraction ratio.

The boundary layer under investigation is developed on the floor of the wind tunnel and transition to a stable turbulent flow is triggered by a 1 in. wide strip of medium grit sand paper which is glued to the floor across the entire span upstream at the entrance of the working section, to obtain a fully developed turbulent boundary layer at the measuring location 22 ft downstream for the test velocity of 3.2 m s^{-1}. The friction coefficient c_f computed from these tests agreed with the values obtained from Clauser charts and Preston tube measurements. It was evaluated at several Reynolds numbers in the working section and a plot of these values against the Reynolds number based on the momentum thickness θ is shown in Andreopoulos & Agui (1996). The principal parameters of the flow are stated in table 1.

The probe, shown schematically in figure 2(*a*), consists of a set of three individual triple-hot-wire sensors put together so that the probe remains geometrically axisymmetric. Each sensor of the triple-wire array is mutually orthogonal to other two, and thus oriented at approximately 54.7° to the probe axis. Each of the 2.5 μm diameter tungsten sensors is welded onto two individual prongs which have been tapered at the tips down to about 40 μm. Thus each sensor is operated independently since no common prongs are used.

The hot-wire output voltage E is related to velocity, U_{eff}, 'as seen by the sensor'

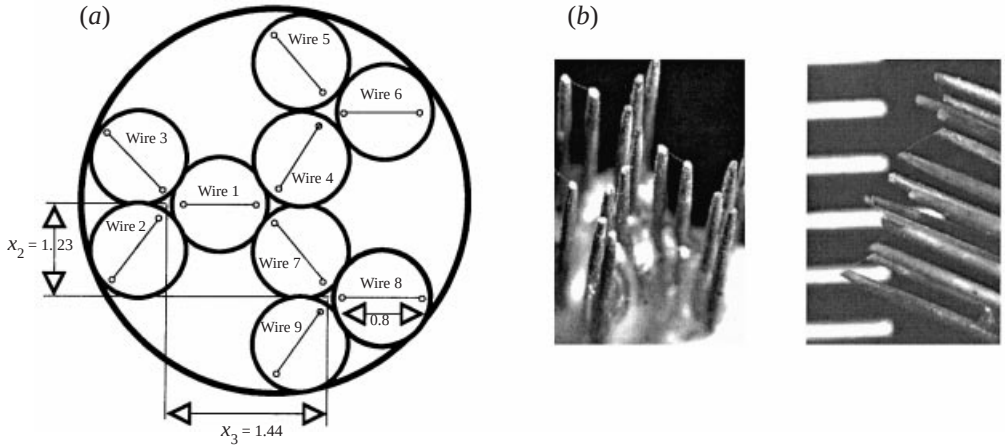

FIGURE 2. (*a*) Sensor arrangement and probe dimensions in mm. (*b*) Photograph of probe.

through the well-known King's law:

$$E^2 = A + BU_{eff}^n. \tag{4.1}$$

The effective velocity is related to U_N, U_T and U_B, the normal, tangential and binormal components of the velocity vector respectively, by what is known as Jorgensen's law:

$$U_{eff}^2 = U_N^2 + k^2 U_T^2 + h^2 U_B^2, \tag{4.2}$$

where k and h are yaw and pitch coefficients. Details of the techniques associated with the use of triple-wire probes can be found in Andreopoulos (1983*a*), while estimates of errors related to probe geometry and turbulence intensity are described in Andreopoulos (1983*b*).

In selecting the vorticity probe dimensions several considerations had to be taken into account during the design process:

(i) The individual wire length l_w should be as small as possible so that small scales can be resolved adequately (see Wyngaard 1969). The length of the wires is also constrained by the conflicting requirement to minimize heat conduction effects to the prongs which demands large l_w/d ratio, where d is the wire diameter.

(ii) The size of the individual triple hot-wire array, l_p should be as small as possible to satisfy the assumption that the velocity is uniform across each wire of each array. Small wire spacing however can lead to thermal interference and cross-talk between the wires.

(iii) Since vorticity or strain rate will be computed from velocity gradients, spacing of the individual probes should be finite so that velocity gradients do not disappear. If this spacing becomes small the effect of noise may overwhelm the signal (see, Antonia, Zhu & Kim 1993 and Wallace & Foss 1995).

(iv) Each of the wires should be controlled independently from the others. The use of one common prong, as in the case of Balint *et al.* (1991), and Vukoslavcevic, Wallace & Balint (1991), may create problems such as imbalance under dynamic conditions.

(v) The transfer function of the hot-wire/anemometer system should be three dimensional. This suggests that the probe should be able to respond to yaw and pitch angle variations of the velocity vector in addition to its magnitude. Very often King's law is confined to contributions from one or two velocity components only. While this assumption simplifies computations and is adequate for measurements in

flows with low turbulence intensity, it is inadequate for measurements in flows with relatively high turbulence intensity. Very close to the wall, fluctuations of all three velocity components are very high and their magnitude is about the same in all three directions. Neglecting contributions from one or two velocity components may lead to very large errors in the measurements of turbulence (see Tutu & Chevray 1975).

The dimensions of the probe which were finally adopted are shown in figure 2(*a*). A photograph of the entire probe assembly is shown in figure 2(*b*).

The probe required additional prongs to operate each sensor independently, which increased only minimally the blockage effects due to the six extra prongs, by about 2.5% over that of Balint *et al.* (1991). Note that their probe uses 12 prongs by making one common to a set of three hot-wires. The present probe, due to the mutually orthogonal orientation of wires, has a larger 'acceptance cone' when compared to the probe of Balint *et al.* (1991), which has one wire at 45° to the plane of the other two orthogonal wires, and therefore the individual triple wire probe is capable of measuring flows with larger turbulence intensities.

In order to compute all three vorticity components, and the six distinct terms of the rate-of-strain tensor, six velocity derivatives need to be evaluated from the three velocity components measured at the three locations, which are at the centres of each of the three triple wires. If these velocity vectors are known then the derivatives can be evaluated. A brief description of the computations of velocity gradients and numerical techniques used in the present investigation is given in the Appendix. The basic assumptions made in these computations is that the flow velocity remains uniform across each wire but it can change across the hot-wire arrays in a linear fashion. An iterative numerical scheme was developed to solve the system of available equations efficiently. Performance data of the scheme are shown in HA. Details of calibration techniques can be found in Honkan & Andreopoulos (1993).

The hot-wire sensors of the vorticity probe were operated by nine channel constant-temperature anemometers, model 56C0l /Cl 7 manufactured by Dantec Electronics Inc. Two analog filters each with eight input channels and an integrated programmable gain amplifier (model Filter 488/8) made by I0tech were used to low-pass filter the anemometer output voltage signals before digitization. Data acquisition hardware consisted mainly of two 16-bit (1 part in 60 000) resolution high performance analog and digital interfaces model ADC488SA manufactured by I0tech. The board has a/d conversion rate of 100 000 samples per second. On board simultaneous sample and hold circuitry allowed simultaneous acquisition of all channels of data.

In-situ calibrations of the probe were carried out in the inviscid free-stream of the flow, once prior to the data acquisition session and again at the end of the experiment. The probe was placed in the middle of the working section by using a 3 ft slender arm which was a part of a computer-controlled three-dimensional traversing mechanism. Extensive yaw and pitch response measurements for each of the sensors were then obtained by elegant coordination of data acquisition on one microcomputer while performing required yaw or pitch rotations through motion control hardware interfaced to another microcomputer. The range of angles covered was $-30°$ to $+30°$, in steps of 5° for both yaw and pitch for five different free-stream velocities.

Data were collected simultaneously on all nine wires with a sampling rate of 5 kHz per channel for total duration of about 82 s at each point. This was adequate according to the criteria given by Klewicki & Falco (1990) for statistical convergence of ensemble quantities. The signals were low-pass filtered at 1 kHz before digitization.

Estimates of spatial resolution of flow scales of the multi-wire probe non-

dimensionalized by the Kolmogorov viscous length scale $\eta = (\nu^3/\varepsilon)^{1/4}$ (Kolmogorov 1941) are presented in HA. These estimates, which depend on the method used to compute the dissipation rate ε, indicate a probe resolution of 4η to 7η in the measurements of velocity gradients at $x_2^+ = 12.5$ which is the measurement location closest to the wall. The spatial resolution of each of the individual wires appears to be in the range of 2η to 4η. These estimates of spatial resolution suggest a possible attenuation of the measured velocity gradient fluctuations which could be of the order 8% according to the analysis of D. W. Ewing & W. K. George (1994, personal communication).

Uncertainty analysis presented in HA indicated that the probe is capable of measuring mean velocity gradients within 12% in the inner-wall region and within 1% in the free stream. The overall uncertainty achieved in the measurements of the fluctuating velocity gradient depends also on the way the statistical averages are non-dimensionalized. If inner-layer scaling is used, then the relative uncertainty $\Delta F/F$ appears to be 10% in the viscous sublayer and buffer region and 20% in the logarithmic region. If outer-layer scaling is used, the relative uncertainty is 5% in the viscous sublayer, 6% in the buffer region and 18% in the logarithmic region. If these uncertainties are expressed relative to the maximum value of the wall mean vorticity their estimates are reduced.

5. Results

5.1. *Comparisons with existing statistical data*

A detailed evaluation of the data obtained with the present multi-wire probe is presented in HA, where statistical averages are compared with previously published experimental and computational results. These comparisons included data of several statistical quantities of fluctuations of the three velocity components, the three vorticity components, all the elements of the strain-rate tensor and the dissipation rate. The comparisons indicated that the performance of the multi-wire probe was very satisfactory. Evidence was also presented in HA suggesting that the probe performs very well in the high-mean-shear, near-wall region where fluctuations of the velocity vector are substantial because of its larger acceptance cone. Some additional comparisons are presented in the following.

Figure 3(*a*) shows the distribution of the turbulent kinetic energy $1/2(u_i u_i)^+$ across the boundary layer. The distance from the wall, x_2, is non-dimensionalized by the boundary layer thickness δ. The present data are compared with the experimental data of Balint *et al.* (1991) and Klebanoff (1954) as well as with the DNS data of Spalart (1988). It should be mentioned that the experimental data of Balint *et al.* were obtained by very similar experimental methods and at $Re_\theta = 2685$ which is very close to the present $Re_\theta = 2790$, while Kelbanoff's (1954) data were obtained at $Re_\theta = 7600$ and the DNS data of Spalart (1988) at $Re_\theta = 1410$. It appears that there is a very satisfactory agreement between the present data and those of Balint *et al.* There is also good agreement in the outer part of the boundary layer with those of Klebanoff and Spalart. Similarly good agreement of the present $(u_1 u_2)^+$ shear stress data is observed with those of Balint *et al.*, Klebanoff and Spalart (see figure 3*b*). However, some deviations start to be noticeable when inner-layer scaling is used. Figure 3(*c*) shows the kinetic energy distribution plotted across the boundary layer in inner-layer scaling. The present data agree quite well with those of Balint *et al.* in the upper end of the buffer region and the logarithmic region, and with the data of Lemonis (1995) in the outer-layer which were obtained at $Re_\theta = 6450$. In the lower half of the

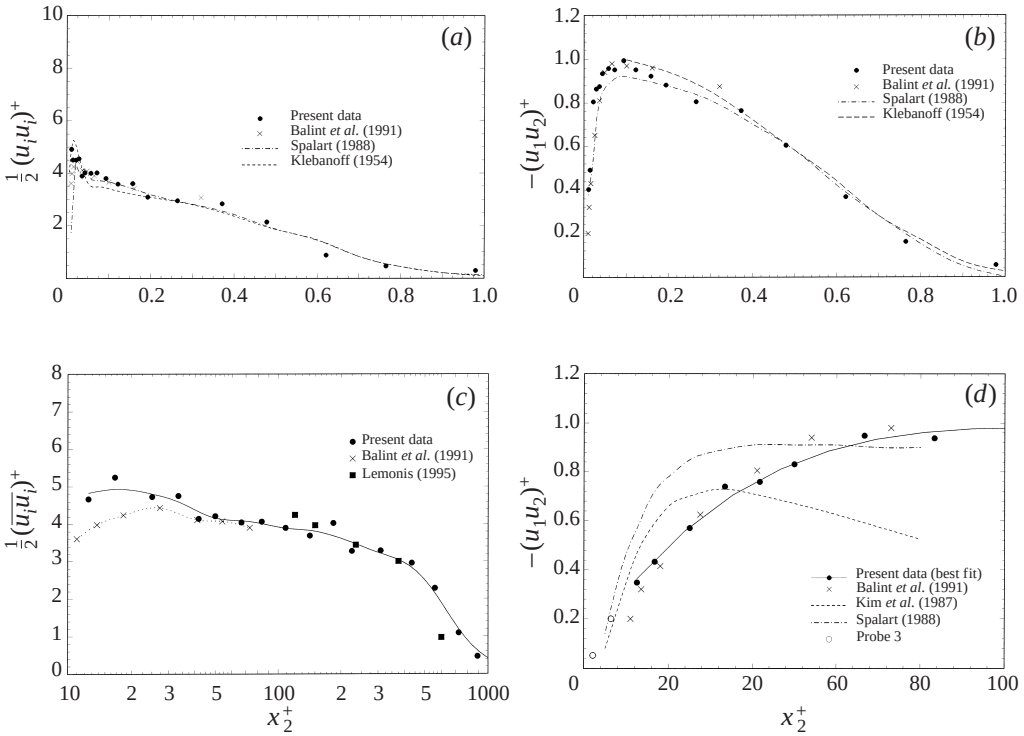

FIGURE 3. Distribution of (*a*) turbulent kinetic energy across the boundary layer, (*b*) shear stress across the boundary layer, (*c*) shear stress across the boundary layer in inner-wall variables, and (*d*) shear stress in the near-wall region.

buffer region the data of Balint *et al.* are lower than the present ones. This difference could be attributed to a greater number of velocity vectors being validated in the present work as a result of a larger acceptance cone of the probe. Better agreement between the present results and those of Balint *et al.* in the highly sheared region near the wall can be observed when the $(u_1u_2)^+$ data are considered. Figure 3(*d*) shows this comparison. The DNS data of Spalart (1988) and Kim *et al.* (1987) which were obtained at a lower Re_θ than the present one appear to be higher than both experimental data sets in the region below $x_2^+ = 35$ and lower in the region above.

Comparison of the measurements of mean turbulent enstrophy $1/2(\omega_i\omega_i)^+$ across the boundary layer with the measurements of Balint *et al.* (1991) obtained at about the same Re_θ is shown in figure 4. In addition, the enstrophy measurements of Lemonis (1995) at $Re_\theta = 6450$ and of Ong & Wallace (1998) at $Re_\theta = 1070$ are also plotted for comparison. The present data of enstrophy agree remarkably well with the measurements of Balint *et al.* (1991) and Ong & Wallace (1998), which are restricted to the near-wall region below $x_2^+ = 75$. Unfortunately there are no measurements in the outer layer of the boundary layer. The measurements of Lemonis (1995) have been carried out in the outer layer only at $Re_\theta = 6450$ and therefore cannot be directly compared with the present ones. They indicate, however, possible Re_θ effects, namely a reduction of vorticity fluctuations with increasing Re_θ. The boundary layer DNS data of Spalart (1988) and the channel flow DNS data of Moser, Kim & Mansour (1999) obtained at lower Re_θ, are also plotted on figure 4 although they cannot be directly compared with the present experimental results.

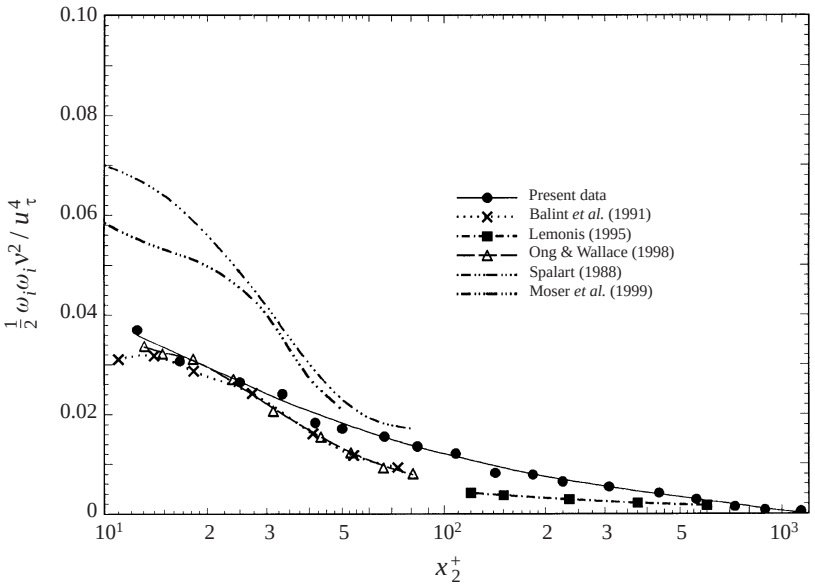

FIGURE 4. Enstrophy distribution across the boundary layer.

Reynolds number effects (see Andreopoulos *et al.* 1984) and the slow relaxation of boundary layer flows to wall disturbances used for tripping the flow (see Andreopoulos & Wood 1982) may be the reasons for the minor differences between the various data sets. Ong & Wallace (1998) attribute a large part of the differences between the experimental data of Balint *et al.* and DNS data of vorticity to an apparent overestimation of u_τ in the experiments, which is raised to the fourth power. Ong & Wallace's data corrected for this overestimation agree quite well with the DNS results. If the present data were corrected for similar effects they would also agree very well with the DNS results. Nevertheless, no correction has been applied to the present data.

The comparisons of the present data of velocity and vorticity statistics with experimental data obtained by other investigators which have been presented in this section as well as in HA and Honkan (1994), indicate that the overall performance of the probe is very satisfactory. In particular the good agreement of vorticity statistics with the data obtained in similar and comparable experiments by Balint *et al.* gives an indication that the overall accuracy of the measurements is very reasonable. This also provides confidence in the quality of the time-dependent data of the velocity gradient tensor, which ensures reliability of the results obtained by further analysis.

5.2. *Statistical characteristics of the velocity and vorticity fields*

The cross-correlation between two components of the vorticity or velocity vectors is always of interest. The best way to identify any possible correlations is by considering the correlation coefficient defined as $Cq_iq_j = \overline{q_iq_j}/q_i'q_j'$ where q_i is a fluctuating component in the i-direction and q_j is a fluctuating component in the j-direction and q_i' and q_j' are the r.m.s. values of these components respectively.

Figure 5 shows the distributions of the correlation coefficients $C\omega_1\omega_2$, $C\omega_1\omega_3$, $C\omega_2\omega_3$ and Cu_1u_2 across the boundary layer. Symmetry considerations and invariance in the spanwise direction of all average quantities require that the cross-correlation $\overline{\omega_1\omega_2}$ is the only non-zero correlation between the fluctuating vorticity components;

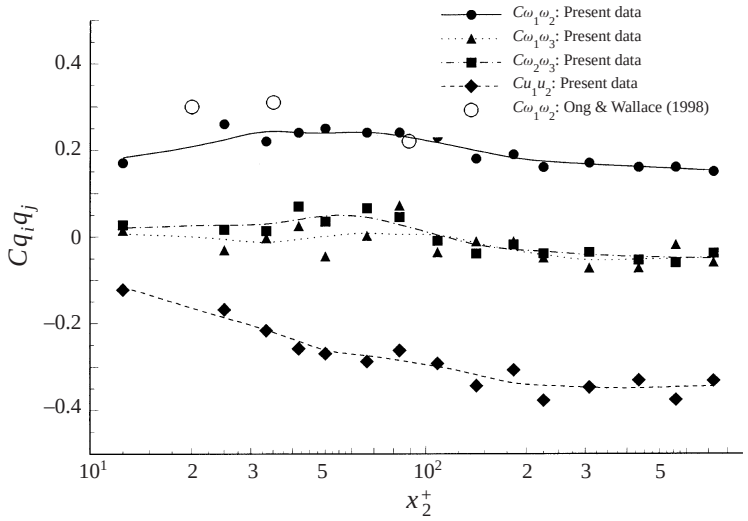

FIGURE 5. Cross-correlation coefficients of vorticity and velocity fluctuations.

the low values of $C\omega_1\omega_3$ and $C\omega_2\omega_3$ measured across the boundary layer confirm this. $C\omega_1\omega_2$ reaches positive values between 0.2 and 0.27 almost everywhere. This suggests a preference of the vorticity vector to have the two components ω_1 and ω_2 of the same sign most of the time. For comparison, the velocity correlation coefficient Cu_1u_2 is also plotted in figure 5. It reaches negative values between -0.12 to -0.4, which is the range found by other investigators. This negative correlation suggests that the two velocity components u_1 and u_2 have opposite signs most of the time. It is interesting to observe that the level of correlation between the two vorticity components is lower than that of the two velocity components. This difference is most likely due the size of the eddies which contribute most to the fluctuations of each of the two quantities. Vorticity contributions come mostly from small eddies while the velocity fluctuating field is characterized by contributions from larger eddies. It appears that any correlation decreases with increasing contributions from smaller eddies. This also explains why any correlation is reduced when the spatial resolution of the measuring probe is enhanced. It should be also noted that the present measurements of the cross-correlation coefficient agree rather well with some limited data of $C\omega_1\omega_2$ found in the paper by Ong & Wallace (1998).

One of the most interesting features of the vorticity field is that the amplitude of its fluctuations is substantially larger than its mean value. The r.m.s. value of the fluctuations, for example, is very often greater than or equal to the mean vorticity. This is evident if the intensity of vorticity fluctuations is considered. Data of the intensity of the spanwise fluctuations, for instance, $\omega_3'/\overline{\Omega}_3$ across the boundary layer are plotted in figure 6. It appears that the major feature of the distribution of the intensity of vorticity fluctuations is that $\omega_3'/\overline{\Omega}_3$ reaches considerably higher values than the corresponding turbulence intensity and that its maximum value occurs not at or near the wall but at about $x_2^+ \simeq 90$. Values as high as 3 at the beginning of the logarithmic layer and as low as 0.45 in the outer layer can be found. These values are about 10 times higher than the corresponding values of the turbulence intensity $((1/2)u_iu_i)^{1/2}/\overline{U_1}$ in the same flow. The shape of the distribution shown in figure 6 is dominated mainly by the distribution of mean Ω_3 across the boundary layer. Mean Ω_3^+ reaches a value of -1 at the wall and close to a zero negative value in the outer

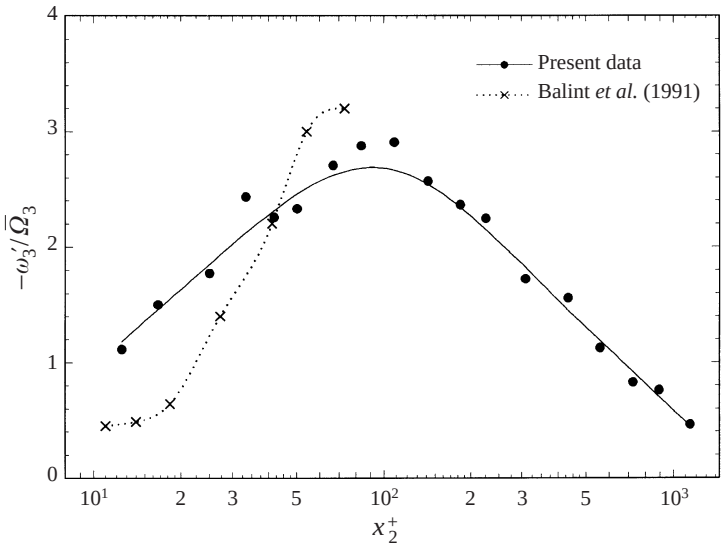

FIGURE 6. Intensity of vorticity fluctuations across the boundary layer.

layer. The r.m.s. values, ω_3' are greater at the wall and in the near-wall region where measurements were possible and diminish in the outer layer. The rate of decrease with increasing distance from the wall in the outer layer is somewhat faster than that of the mean vorticity $-\Omega_3^+$ so that the ratio $\omega_3'/\overline{\Omega_3}$ goes to zero and not to infinity.

The present data are also compared to those of Balint *et al.* Qualitatively, both data sets show the same trends. Their quantitative difference is mainly due to the difference in the values of mean vorticity, Ω_3^+, since the ω_3' values agree reasonably well, as has been pointed out in HA. The present measurements of mean vorticity in the buffer region follow closely the theoretical distribution. $\overline{\Omega_3} = A(x_2^+)^3 - 1$ of Bradshaw & Huang (1995) where $A = 1.4 \times 10^{-3}$ according to Mansour, Kim & Moin (1988). Balint *et al.*'s data agree with Spalding's (1961) formula. These two theoretical distributions are not identical. Thus, these small differences between small values of mean vorticity in the two data sets are enough to introduce the quantitative disagreement shown in figure 6.

The importance of the kinematic shear stress $\overline{u_1 u_2}$ in identifying organized motions in turbulent flow has been recognized since the work of Bradshaw, Ferris & Atwell (1967) and Townsend (1976). One aspect of this shear stress, which has attracted rather little attention, is the large magnitude of the amplitude of its fluctuations about its mean value. This is evident in some of the statistical properties of the fluctuations which were evaluated in the present analysis, particularly in their r.m.s. statistics across the boundary layer which have been computed and are plotted in figure 7. Values of r.m.s. up to 2 in wall viscous units can be observed in the region $35 < x_2^+ < 300$. These values, which agree rather well with the old measurements of Gupta & Kaplan (1972), are about 3 times the local mean shear stress value. This indicates that, very often, mean values of shear stress and, to a certain extent, consideration of time-average terms in the Navier–Stokes equations, can be very misleading in the understanding of the physical aspects of the flow structure.

Figure 8 shows the distribution of the mean values of the three components of the vorticity stretching vector $S_{ik}\Omega_k$. The stretching term is a source/sink term in the transport equation of vorticity and, in the absence of substantial viscous effects,

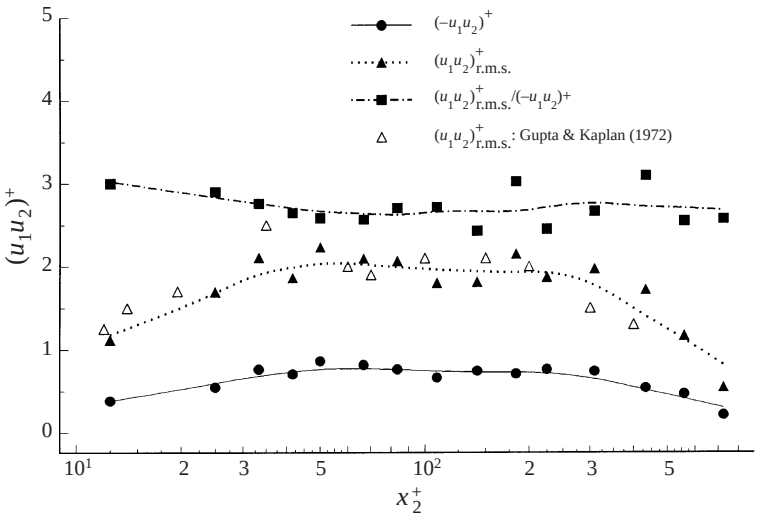

FIGURE 7. Shear stress fluctuations across the boundary layer.

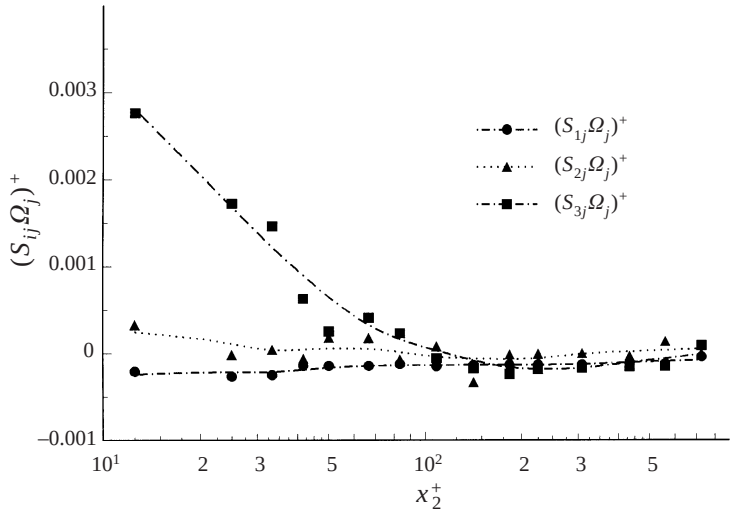

FIGURE 8. Mean stretching components across the boundary layer.

it represents the net change of vorticity in a Lagrangian frame of reference. The instantaneous total stretching term $S_{ik}\Omega_k$ is related to the instantaneous turbulent stretching term $s_{ik}\omega_k$ through the relation $S_{ik}\Omega_k = \overline{S_{ik}}\ \overline{\Omega_k} + s_{ik}\overline{\Omega}_k + \overline{S_{ik}}\omega_k + s_{ik}\omega_k$. Time-averaging yields $\overline{S_{ik}\Omega_k} = \overline{S_{ik}}\ \overline{\Omega_k} + \overline{s_{ik}\omega_k}$. In the present case of a two-dimensional boundary layer the first term on the right-hand side is zero and therefore it appears that $\overline{S_{ik}\Omega_k} = \overline{s_{ik}\omega_k}$. Symmetry and invariance of averages in the spanwise direction requires that stretching in the spanwise direction, $\overline{S_{3k}\Omega_k} = \overline{s_{3k}\omega_k}$, is the only non-zero component. The data in figure 8 indicate that this term reaches significant values very close to the wall. As the distance x_2^+ from the wall increases, the stretching decreases, and in the region $x_2^+ > 100$, its value is negligible. The present data of the other two vorticity components show very small values throughout the boundary layer, as they should be since they are expected to be zero. However, the r.m.s.

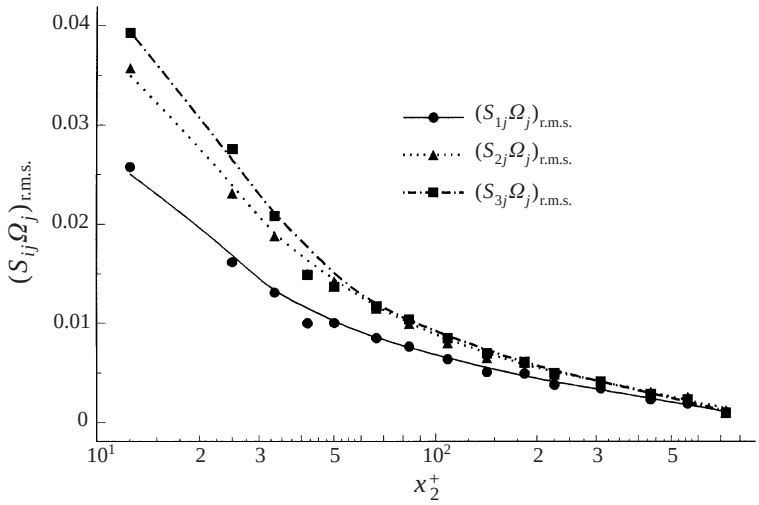

FIGURE 9. Distributions of r.m.s. of fluctuations of stretching components across the boundary layer.

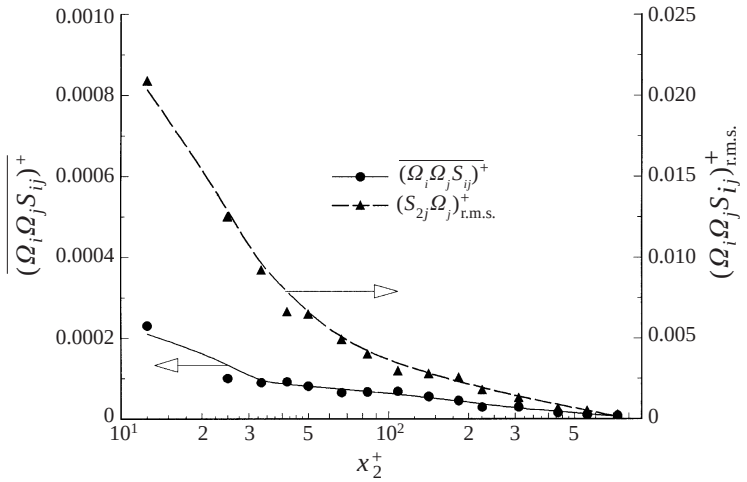

FIGURE 10. Enstrophy generating term $\Omega_k\Omega_i S_{ik}$ across the boundary layer.

values of all the stretching vector components are very significant, and in fact they reach values one order of magnitude larger than the mean spanwise component. This is shown in figure 9. High-amplitude fluctuations are evident very close to the wall and low-amplitude fluctuations in the outer part. This is another feature of the fluctuations in addition to their large amplitude, namely that they are present throughout the boundary layer while their mean spanwise stretching component is significant only in the region $x_2^+ < 100$. It should be noted that the fluctuations of the total stretching term $S_{ik}\Omega_k$ about its mean value $\overline{S_{ik}\Omega_k}$ are different from the fluctuations of turbulent stretching term $s_{ik}\omega_k$ about its mean value $\overline{s_{ik}\omega_k}$ through the relation $(S_{ik}\Omega_k - \overline{S_{ik}\Omega_k}) = (s_{ik}\omega_k - \overline{s_{ik}\omega_k}) + s_{ik}\overline{\Omega}_k + \overline{S_{ik}}\omega_k$. The presence of the last two terms in this relation prohibits $(S_{ik}\Omega_k)_{\text{r.m.s.}}$ from being the same as $(s_{ik}\omega_k)_{\text{r.m.s.}}$. The contribution of these two terms, however, appears to be relatively significant only at the three measurement locations very close to the wall.

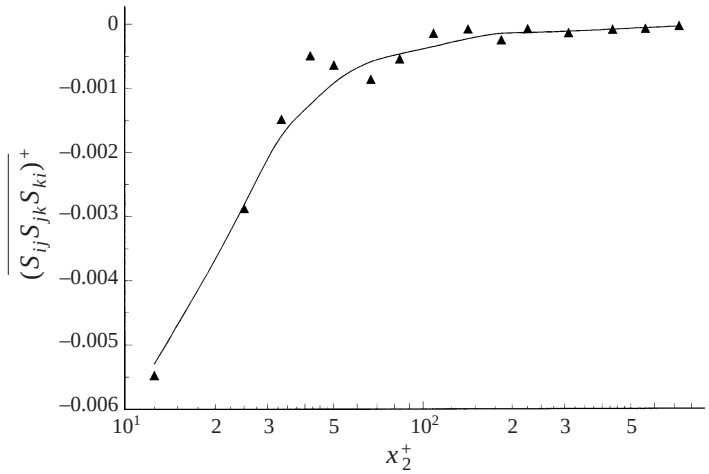

FIGURE 11. Distributions of mean values of $S_{ij}S_{jk}S_{ki}$ across the boundary layer.

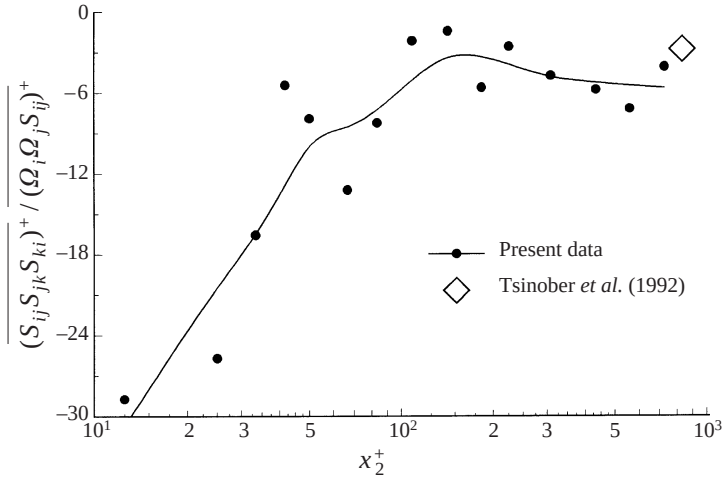

FIGURE 12. Distribution of the ratio $\overline{S_{ij}S_{jk}S_{ki}}/\overline{\Omega_i\Omega_k S_{ik}}$ across the boundary layer.

As mentioned earlier, the instantaneous enstrophy is the second invariant of the rotation-rate matrix R_{ij}. The first two terms on the right-hand side of its transport equation (3.6) are source/sink terms describing the generation or destruction of enstrophy by the strain S_{ik} through rotation and stretching or compression of vortex lines. These enstrophy-generating terms can be expressed in terms of vorticity as $\Omega_k\Omega_i S_{ik}$. The time-average value of this very important quantity in the dynamics of turbulent flows was found by Tsinober *et al.* (1992) to be always positive in grid-generated turbulence, indicating the prevalence of vortex stretching over compression. Figure 10 shows the distribution of the mean and r.m.s. values of $\Omega_k\Omega_i S_{ik}$ across the boundary layer. Both quantities reach larger values very close to the wall and low values in the outer layer. The most striking feature, however, is that the level of the r.m.s. values is about 100 higher than the corresponding mean value at the same location. This is further evidence indicating that very few physical aspects can be explored through the time-average enstrophy equation.

Mean values of the term $S_{ij}S_{jk}S_{ki}$ across the boundary layer are shown in figure 11.

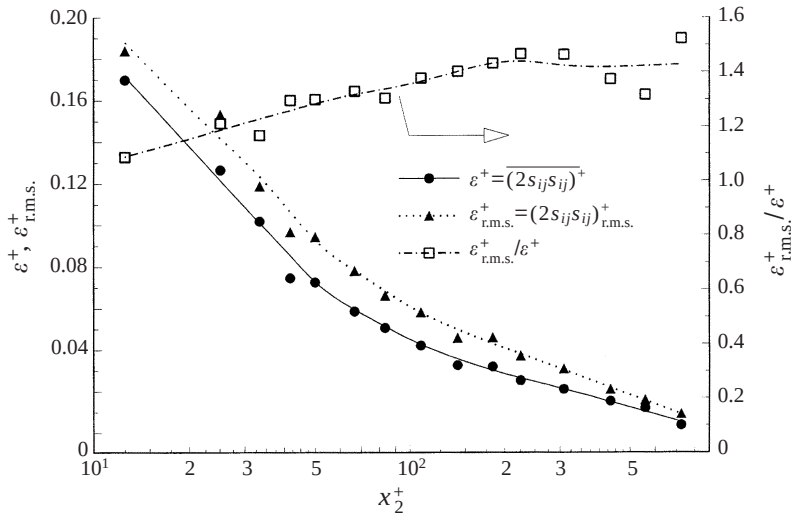

FIGURE 13. Mean and r.m.s. values of dissipation rate across the boundary layer.

This is one of the two source/sink terms in the transport equation (3.11) of the total dissipation $S_{ij}S_{ij}$. The other term appears to be the previously discussed term $\Omega_k\Omega_iS_{ik}$ shown as $R_{jk}R_{ki}S_{ij}$ in equation (3.11). Large negative values of $\overline{S_{ij}S_{jk}S_{ki}}$ are reached in the near-wall region while values close to zero are evident for $x_2^+ > 100$. It is also interesting to observe that this term is always larger than the $\Omega_k\Omega_iS_{ik}$ term. Figure 12 shows the ratio of these two quantities $\overline{S_{ij}S_{jk}S_{ki}}/\overline{\Omega_i\Omega_kS_{ik}}$. In ideal homogenous flows this ratio reaches values close $-3/4$ according to Townsend (1951). The present data show values close to -30 near the wall as a result of the strong non-homogeneity of the flow in this region, and much less in the region $x_2^+ > 100$. Tsinober *et al.* (1992) have quoted a value of -2.4 of this ratio at $x_2/\delta = 0.2$ which corresponds to about $x_2^+ = 840$. This value is close to the present measurements in the outer layer of the flow. Both $\overline{S_{ij}S_{jk}S_{ki}}$ and $\overline{\Omega_i\Omega_kS_{ik}}$ eventually obtain negative values in the transport equation of $S_{ij}S_{ij}$, i.e. they tend to reduce dissipation. The first term, however, is overwhelmingly larger than the second one throughout the boundary layer, particularly in the region near the wall.

5.3. *Rates of dissipation and production of turbulent kinetic energy*

Figure 13 shows the distribution of the mean values of the dissipation rate of the turbulent kinetic energy, $\varepsilon^+ = (2s_{ij}s_{ij})^+$ across the boundary layer. The r.m.s. values of its fluctuations about its mean are also plotted in figure 13. The r.m.s. values presented here appear to be of the same magnitude as the mean values. In fact, their ratio $\varepsilon^+_{\text{r.m.s.}}/\overline{\varepsilon^+}$, which is also shown in figure 13, reaches values between 1 and 1.6. Thus the dissipation is another quantity which is characterized by large-amplitude fluctuations.

Mean and r.m.s. values of the production of turbulent kinetic energy, as described by equation (3.14), are shown in figure 14. Large values of mean production can be observed in the region $x_2^+ < 100$. The r.m.s. values of the fluctuating part of the production are about 10 times larger than the corresponding mean values in the near-wall region and about 30 times larger in the outer region.

It should be pointed out here that the present data of mean dissipation rate and mean production of turbulent kinetic energy have been compared very satisfactorily

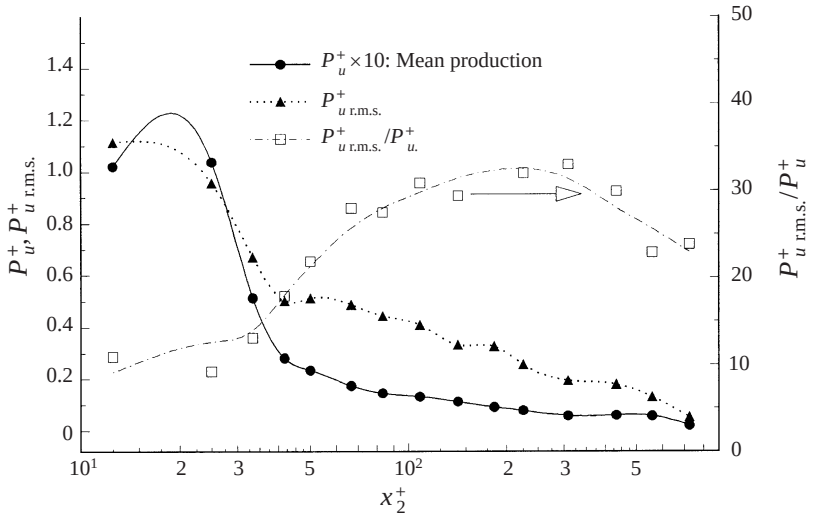

FIGURE 14. Mean and r.m.s. values of production of turbulent kinetic energy across the boundary layer.

with the data of Balint *et al.* (1991) as discussed in detail by HA. In order to keep clarity among the data presented in figures 13 and 14 the data of Balint *et al.* are not re-plotted here.

It is very useful to compare the r.m.s. values of the production of $(1/2)u_iu_i$ with those of the dissipation rate. It appears that the amplitude of the fluctuations of the former is about 10 times larger than the amplitude of fluctuations of the dissipation rate. This is a distinct difference between the production of turbulent kinetic energy and its rate of dissipation, although both are expected to have, according to some theories, mean values very close to each other in the logarithmic region. It should be noted that not only should the time-average terms of the transport equation of $(1/2)\overline{u_iu_i}$ be in balance but also the time-dependent terms of equation (3.13). Thus, the question which remains to be answered is how these large fluctuations of production are balanced out instantaneously. Inspection of the time-dependent signals indicated that the dissipation rate is much more intermittent than the production terms. Bursts of dissipative activities are found which can have amplitudes 10 or more times their r.m.s. values. These large excursions in the $s_{ij}s_{ij}$ signal very often correspond to peaks in the production of kinetic energy, but not always. The signal of the production terms is considerably less intermittent than that of the dissipation and it is very often counterbalanced by advection. Thus, it appears that any excess production of kinetic energy which is not dissipated locally is advected downstream.

The present data of production and dissipation were further analysed by computing their joint probability density function (JPDF). A typical JPDF for the data obtained at $x_2^+ = 12.5$ is shown in figure 15. Both variables are normalized through inner-wall scaling. A peak in the distributions can be observed, which occurs at $\varepsilon^+ = (2s_{ij}s_{ij})^+ = 0.2$ and $P^+ = -0.12$. The distribution is also characterized by long tails. Indicative of the rare but violent bursting activities present in the dissipation signal are the large excursions of the iso-probability contours in the direction of the dissipation axis, which are particularly evident in the low probability contours despite the smoothing applied to them.

Another demonstration of the relation between production of turbulent kinetic

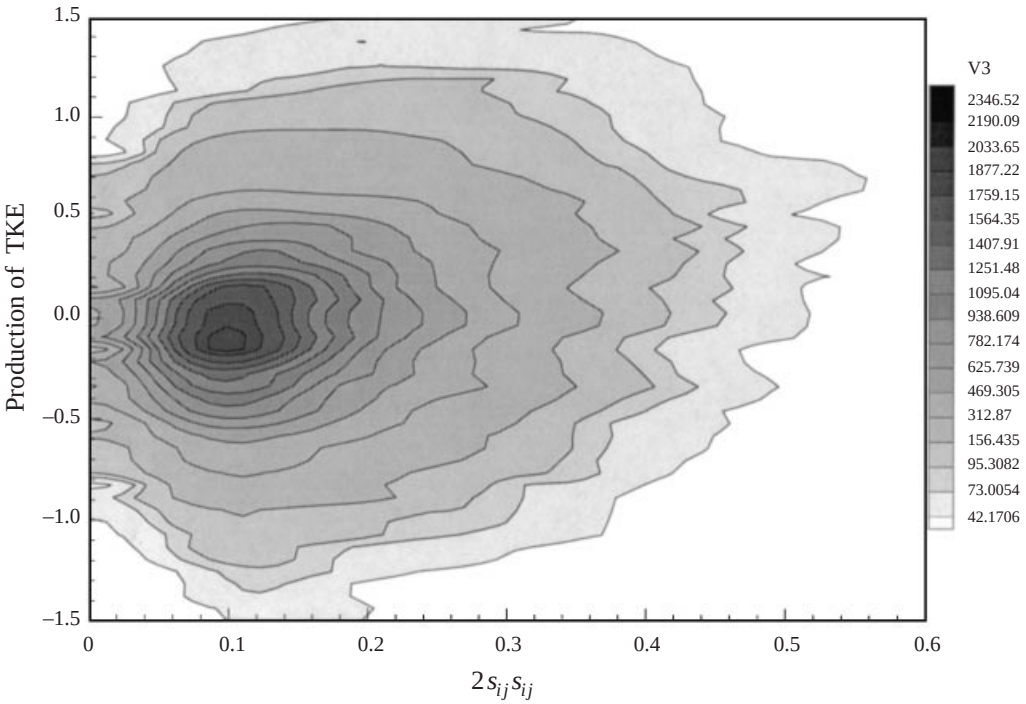

FIGURE 15. Joint probability density function of turbulent kinetic energy and dissipation rate at $x_2^+ = 12.5$.

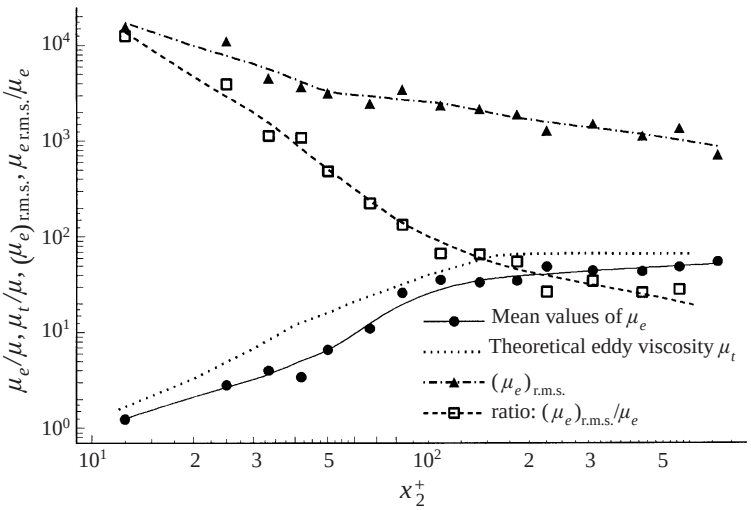

FIGURE 16. Mean and r.m.s. values of momentum exchange coefficient/eddy viscosity across boundary layer.

energy and its dissipation rate can be obtained if the eddy viscosity μ_t is considered. One common definition of μ_t is as $\mu_t/\mu = -\rho\overline{u_iu_j}\overline{S_{ij}}/2\mu\overline{S_{ij}S_{ij}}$ which is very close to the original one from the relation $\rho\overline{u_iu_j} = (1/3)\delta_{ij}\rho\overline{u_iu_i} - 2\mu_t\overline{S_{ij}}$. In the present context, a coefficient of momentum exchange μ_e is defined as the ratio of the instantaneous production of $(1/2)u_iu_i$ as expressed by equation (3.14) to the instantaneous dissipation

rate: $\mu_e/\mu = [-\rho u_i u_j S_{ij} + (\rho u_i u_j - \rho\overline{u_i u_j})s_{ij}]/2\mu s_{ij}s_{ij}$. Thus μ_e can be considered as an instantaneous eddy viscosity coefficient. Mean and r.m.s. values of this coefficient are plotted in figure 16 normalized by the molecular kinematic viscosity of air μ. Mean values of μ_e/μ are of order 1 in the near-wall region and are of the order of 40 in the rest. These values compare very favourably with the theoretical eddy viscosity μ_t/μ values which were obtained by assuming that $\overline{S_{12}^+} = 1$ in the viscous sublayer, $\overline{S_{12}^+} = 1 - A(x_2^+)^3$ in the buffer region with $A = 1.4 \times 10^3$ (see Bradshaw & Huang 1995) and $\overline{S_{12}^+} = 1/(\kappa x_2^+)$ in the logarithmic-law region. In the outer part of the boundary layer, the value of $\mu_t = 0.018\rho U_e \delta^*$ has been used which yields $\mu_t/\mu = 72$. The theoretical mean values were obtained from a ratio of mean values while the mean values of the present experimental data have been obtained by time-averaging the instantaneous ratio of production to dissipation rate ratio. In that respect perfect agreement between these two quantities should not be expected. The r.m.s. values of the μ_e fluctuations appear to be several orders of magnitude greater than its mean values. The ratio between the r.m.s. and the corresponding mean of μ_e is 10^4 in the near-wall region, decreasing fast to 12 in the outer region. These large fluctuations of μ_e also indicate that, depending on the application, time-dependent phenomena may be of greater importance than time-average ones. This further suggests that the use of time-average transport equations may be very misleading in the understanding of the physical processes occurring in turbulent flows.

Most of the quantities considered in the present investigation reach high values in the wall region, which can be approximately defined as $x_2^+ < 80$. Mean stretching $\overline{S_{3k}\Omega_k}$, for instance, as well as $\omega_3'/\overline{\Omega}_3$, $\overline{S_{ij}S_{jk}S_{ki}}$, P^+ and μ_e, show some definitive changes in their distributions at a distance from the wall between $x_2^+ = 60$ and 100. Around this location, the rate of change of any of the quantities considered above with respect to x_2^+ changes distinctly. $\overline{S_{3k}\Omega_k}$, for instance, slows down, $\omega_3'/\overline{\Omega_3}$ reaches a peak and $\overline{S_{ij}S_{jk}S_{ki}}$ reaches a plateau. This observation suggests that most of the intensive vortical or dissipative processes occur in the region closest to the wall. The outer layer is characterized by phenomena weaker in intensity relative to the near-wall, which may be of interest too. Stretching or compression of vortex filaments is evident there as indicated by the strong fluctuations of the stretching vector.

5.4. *The measured invariants*

The JPDF of the two invariants $Q_R = (1/2)R_{ij}R_{ij}$ and $Q_S = -(1/2)S_{ij}S_{ij}$ is shown in figure 17 for the data obtained at $x_2^+ = 12.5$. The mean-value distribution of Q_R has been shown earlier in figure 4, while the mean- and r.m.s.-value distributions of Q_S have been shown in figure 13.

The major characteristic of the JPDF is the long tails of its distribution. The most probable values of $-Q_S$ and Q_R are located close to the point (0.021, 0.020). However, of interest are events with large values of either or both of the invariants which, although having low probability of occurrence, are indicative of significant dynamical processes. The bursting events present in the time-dependent dissipation signal, for instance, which are associated with large-amplitude excursions of the $S_{ij}S_{ij}$ signal, contribute very little to the mean value of dissipation because they do not occur very often, but they are very important because they contribute to the dissipative motions of the small eddies. It is very interesting to see whether these highly dissipative events are associated with large values of enstrophy. Soria *et al.* (1994) have associated the large values of both $-Q_S$ and Q_R with the existence of local shear layers in the flow. These points on the $-Q_S$, Q_R plot are very close to the $-Q_S = Q_R$ line. Events with

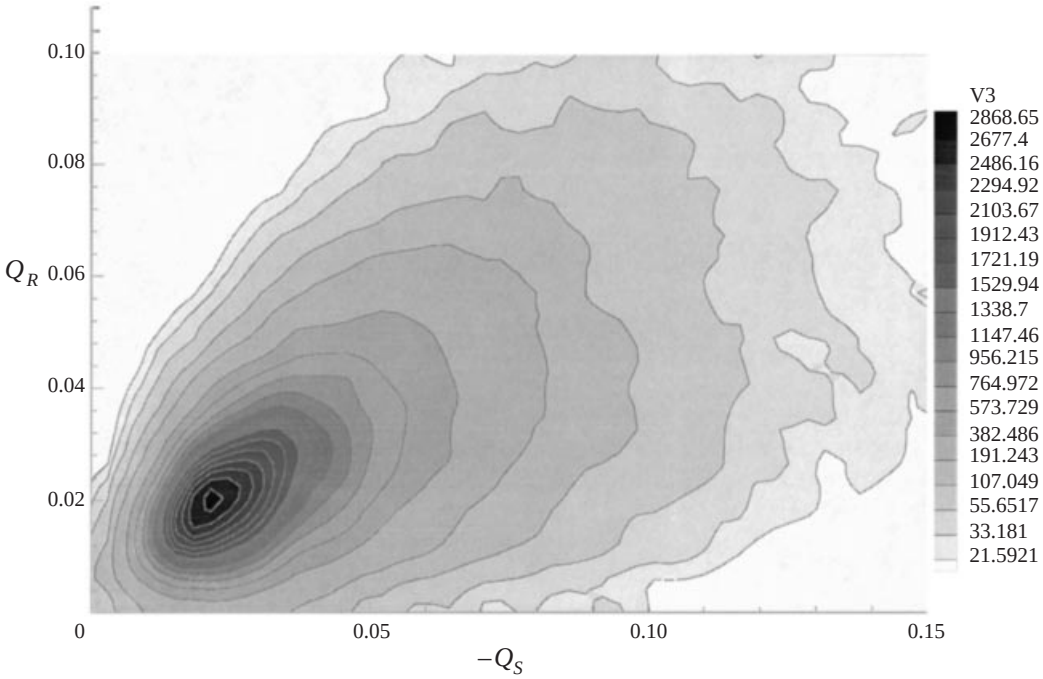

FIGURE 17. Joint probability density function of the $-Q_S$, Q_R invariants at $x_2^+ = 12.5$.

large values of $-Q_S$ and low values of Q_R are indicative of irrotational dissipation, while events with low values of $-Q_S$ and large values of Q_R are indicative of the existence of vortex tubes in the flow.

Contours of the JPDF shown in figure 17 indicate that dissipation dominates the flow motions more than enstrophy. The present data show some weak activity of non-dissipative vortex tubes, while substantial irrotational dissipative motions can be observed. The bulk of the data, however, fall in the region defined by large values of both invariants, which indicates the existence of strong shear layers with a strong degree of flow inhomogeneity since in many cases $-Q_S \neq Q_R$. The ragged contours with low probability at large values of the invariants also suggest the existence of violent events, very likely associated with the passage of shear layers through the measurement location.

Mean and r.m.s. values of the second invariant Q of the velocity-gradient tensor across the boundary layer are shown in figure 18. This invariant is related to $(1/\rho)\nabla^2 P/\partial x_k \partial x_k$ through equation (3.4) and it indicates whether strain or rotation/vorticity dominates locally the dynamical processes, particularly pressure fluctuations. Increased strain may be also associated with outer-layer eddies scrubbing the wall (Kasagi *et al.* 1995) or with eddies 'splashing' on the wall (Wood & Bradshaw 1982). This invariant is also an indicator of the inhomogeneity of the flow, since

$$Q = \tfrac{1}{2}(-S_{ij}S_{ij} + R_{ij}R_{ij}) = -\frac{1}{2}\frac{\partial U_i}{\partial x_j}\frac{\partial U_j}{\partial x_i} = \frac{1}{2}\frac{1}{\rho}\frac{\nabla^2 P}{\partial x_k \partial x_k}.$$

All measured mean values of Q are negative, suggesting on average that strain dynamics dominate pressure fluctuations more than enstrophy. The fact that mean Q reaches larger negative mean values in the near-wall region is also indicative of the

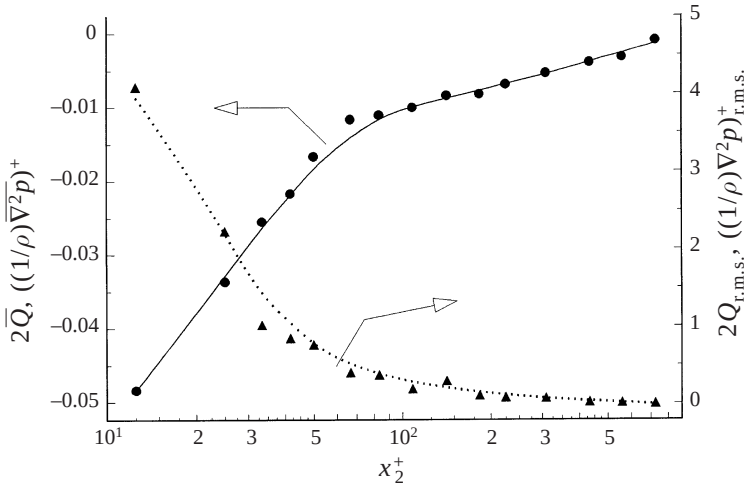

FIGURE 18. Mean and r.m.s. values of the invariant Q across the boundary layer.

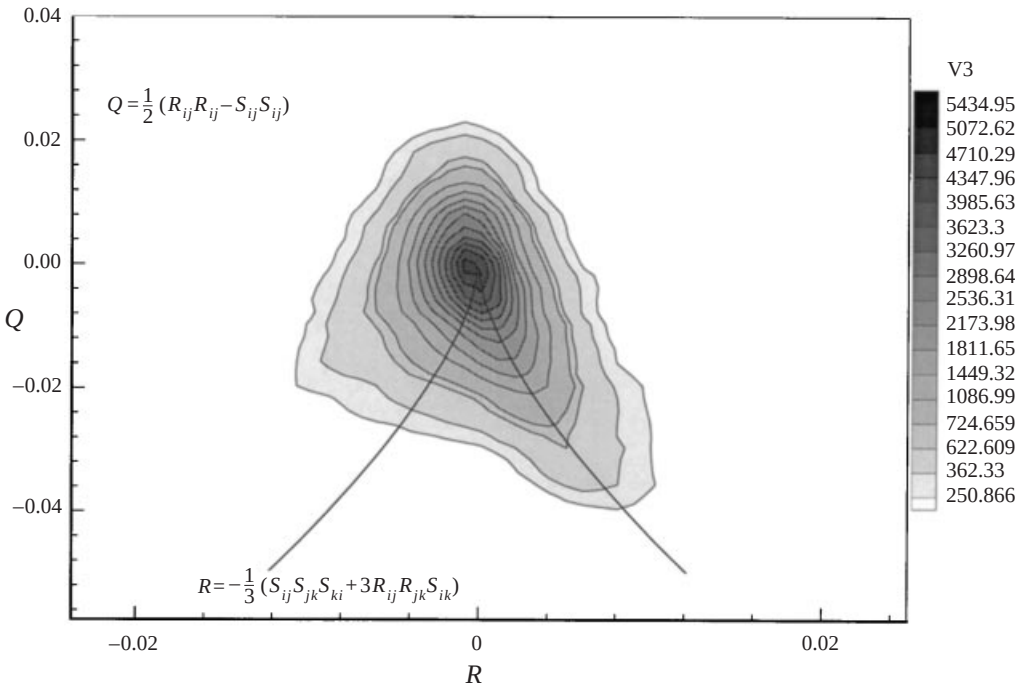

FIGURE 19. Joint probability density function of the Q and R invariants of velocity gradient tensor at $x_2^+ = 12.5$.

flow inhomogeneity there. Values of mean Q approaching zero can be found in the outer region of the boundary layer.

The r.m.s. data of Q shown in figure 18 are also very high near the wall and they are diminishing in the region $x_2^+ > 100$. They reach values which are 100 times larger than the corresponding mean values, which may be indicative of significant dynamical processes taking place in near the wall. This is another characteristic example of how long time-averaging can mask the dynamics of the signals.

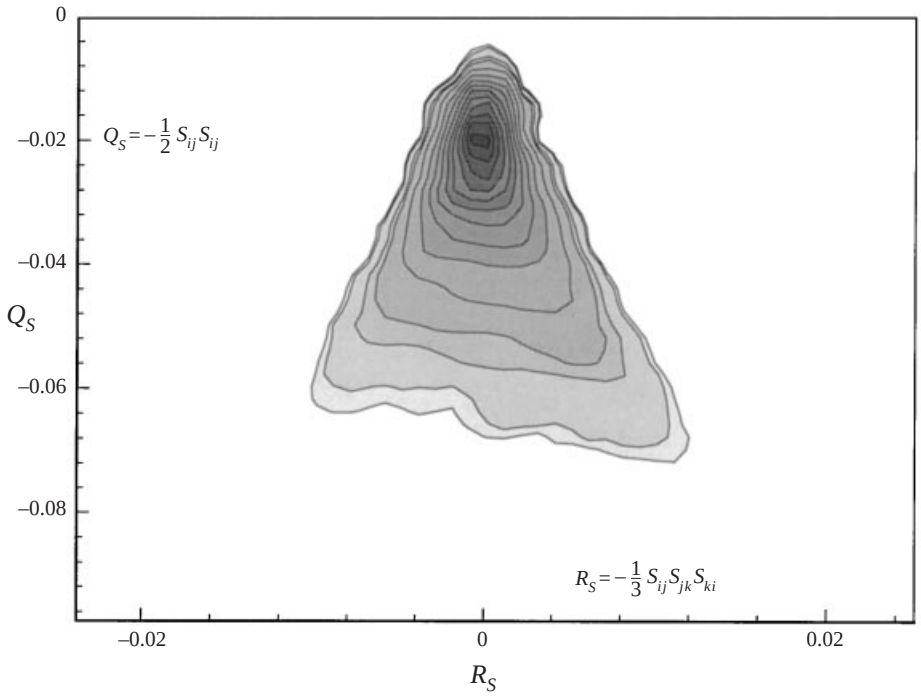

FIGURE 20. Joint probability density function of the Q_S and R_S invariants of strain-rate tensor at $x_2^+ = 12.5$.

The JPDF of the second and third invariants, Q and R respectively, of the velocity gradient tensor is shown in figure 19. It has been computed from the data obtained at $x_2^+ = 12.5$. The axes of the graph, as in the JPDFs presented earlier, are normalized by inner-wall variables. In the same figure the zero value lines of the discriminant D of equation (2.2) are also plotted. These lines define the various regions of the topologies on the plane $P = 0$ of the first invariant.

The most striking feature of the present JPDF is its qualitative agreement with the JPDF of Chaćin *et al.* (1996, figure 4), which has been obtained from the DNS data of Spalart (1988). The present iso-probability contours have a tendency to follow the $D = 0$ line and assume an inverted teardrop shape. The most probable value, however, is near the origin where most of the data cluster. The same exact features can be discerned from the data of Chaćin *et al.* Events which are characterized by large values of Q and R are mostly located in the fourth quadrant, where $R > 0$ and $Q < 0$, and in the second quadrant where $R < 0$ and $Q > 0$. In the first case, with $Q < 0$, the dissipative motions are stronger than the rotational ones and dominate Q. It should be noted that the invariant R consists of two terms which appear as source terms in the transport equation of $S_{ij}S_{ij}$ (see equation (3.11)). Thus, when $S_{ij}S_{ij}$ increase, Q decreases, the source terms increase and therefore R decreases too. In that respect, it appears that there is another relation among the invariants which is defined through one of the transport equations. However, the physical interpretation of the invariants remains with the flow topologies. In this quadrant, the flow topology can be unstable–focus compressing if $D > 0$ or unstable–node saddle–saddle if $D < 0$.

Figure 20 shows the JPDF of the two strain-rate invariants Q_S and R_S at $x_2^+ = 12.5$. These two invariants represent the dissipation rate and its generation term in the

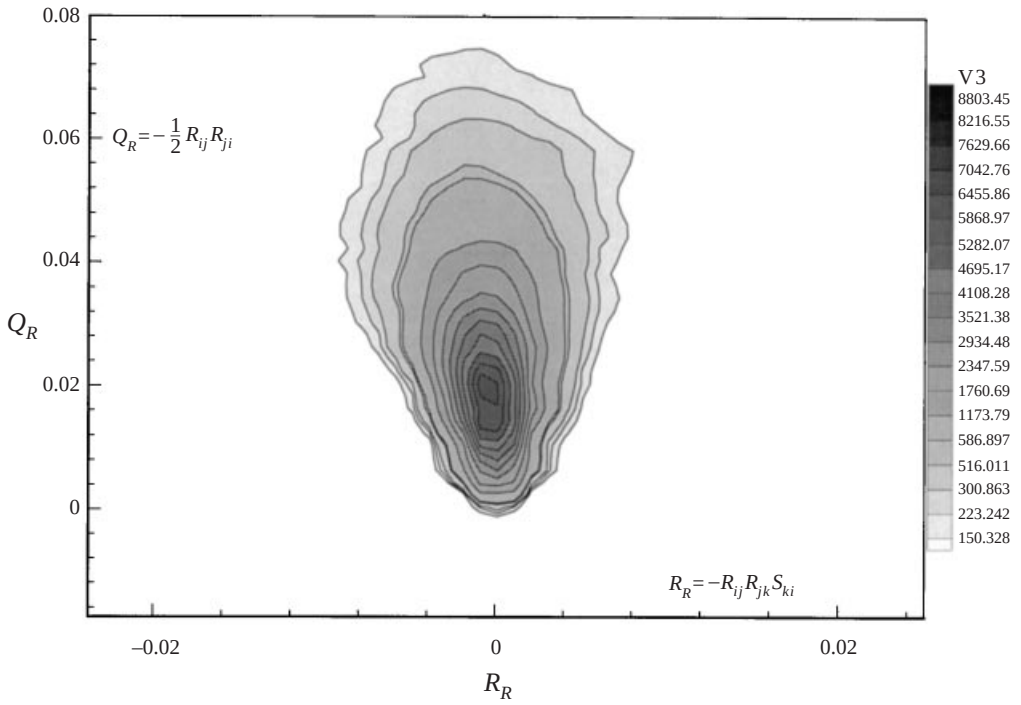

FIGURE 21. Joint probability density function of the Q_R and R_R invariants of rotation-rate tensor at $x_2^+ = 12.5$.

corresponding transport equation (3.11). The data in this figure show that rare events with large values of R_S are also associated with large values of dissipation.

The JPDF between the two invariants Q_R and R_R of the rotation-rate tensor are shown in figure 21. The invariant R_R is also one of the source terms appearing in the transport equation of enstrophy (3.6).

6. The vortex streaks

It has been suggested in the past that the typical near-wall structure of a turbulent boundary layer is a hairpin vortex or a horseshoe vortex (Theodoresen 1952; Smith & Walker 1995; Robinson 1991; Blackwelder & Haritonidis 1983). The study of the kinematics of the near-wall flow by Robinson (1991) showed the existence of asymmetrical hairpin vortices and the presence of individual parts of these vortices like single elongated legs or longitudinal cane vortices. Perry & Chong (1982) and Perry, Henbest & Chong (1986) extended Townsend's (1976) hypothesis of attached eddies to postulate that the near-wall structure consists of a sequence of Λ-shaped vortices which can induce a flow field with a logarithmic-law behaviour. Meinhart & Adrian (1995) observed experimentally the existence of several uniform-momentum zones separated by thin shear layers. This work, as well as the DNS of Liu & Adrian (1999) in channel flows, provided evidence to conceptualize near-wall vortices as groups or packets of several vortices aligned in space so that they generate a low-momentum streak. Measurements of vorticity flux at the wall beneath the boundary layer in our laboratory (see Andreopoulos & Agui 1996) indicated the generation of

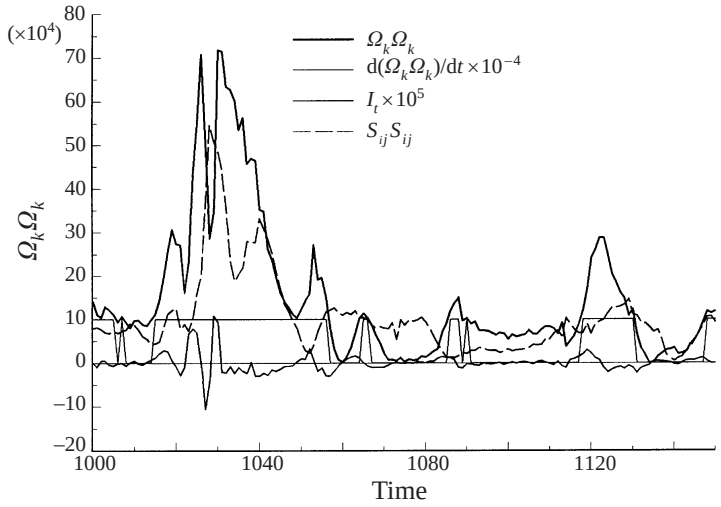

FIGURE 22. Typical signals of enstrophy, its time-derivative and intermittency function at $x_2^+ = 12.5$.

bipolar vorticity at the wall, possibly in the form of mushroom-type vortices, with a rate much higher than the traditionally defined bursting frequency.

In order to provide some additional insight into the fundamental structure near the wall, the present data were further analysed by applying a level threshold to the time-dependent enstrophy signal, $\Omega_k\Omega_k$. The level of this threshold was no more than one r.m.s. of the signal of enstrophy. The signal was then interrogated at each digital point and the value of the intermittency function I_t was determined. I_t was defined as $I_t = 1$ if the amplitude of the instantaneous signal, at a given time, was greater than the threshold value or as $I_t = 0$ in all other cases. In that respect an event was identified as when the amplitude of the signal was above the threshold value. This approach allows consideration of significant vortical motions only, while ignoring all other events with lower amplitude than the threshold. The time duration of these strong events is $T_e = N_e\Delta t$, where N_e is the number of points within the event and Δt is the sampling interval between successive points. The time between two sequential events is designated as $T_b = N_b\Delta t$ where N_b is the corresponding number of points between these strong events.

The enstrophy signals showed, on many occasions, large fluctuations within the time duration, T_e, of a strong event. This may suggest the existence of several vortical filaments inside a strong event. The passage of vortex sheets or shear layers which contain several vortices, for instance, is the best candidate to provide physical interpretation of the strong events detected here with substantial fluctuation of vorticity within. In order to find out how often this vorticity burst/packet or vortex streak phenomenon may take place, the data were further searched to determine the number of local maxima/minima within a strong event. If one assumes that each of these local maxima represents the passage of a vortex filament then the number of these filaments or vortices within a strong event can be estimated. The number of local extremes was calculated by considering the time-derivative of the enstrophy signal $\partial(\Omega_k\Omega_k)\partial t$ and counting its zero crossings. Figure 22 shows a typical time record of the signals considered and the intermittency computed from the algorithm described above. They have been obtained from the measured data at $x_2^+ = 12.5$. In addition, the corresponding signal of $S_{ij}S_{ij}$ is also plotted for comparison. Both $\Omega_k\Omega_k$

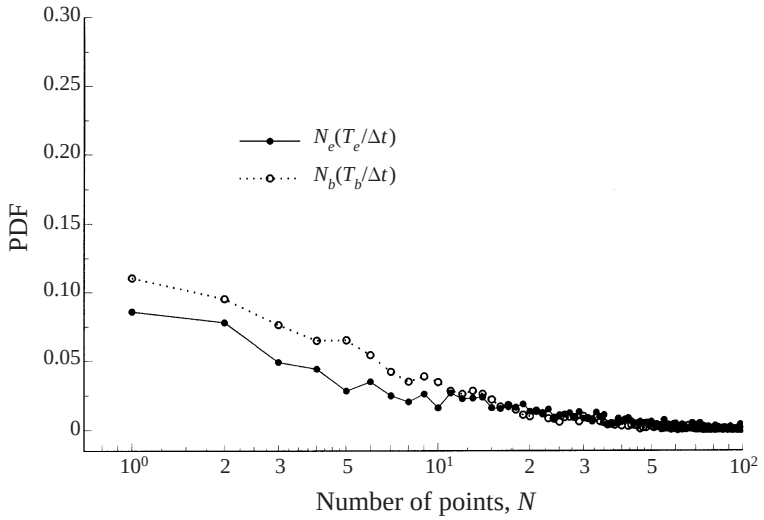

FIGURE 23. Probability density function of duration and appearance of strong vortical events.

and $S_{ij}S_{ij}$ are related to the invariants Q_R and Q_S in equation (3.4). They are also related through $S_{ij}S_{ij} = (1/2)\Omega_k\Omega_k + \partial U_i/\partial x_j \partial U_j \partial x_i$ where the second term on the right-hand side represents contributions from the inhomogeneous part of the flow. Its time-average value is zero in homogeneous and isotropic flows. It is this term which prevents $S_{ij}S_{ij}$ and $(1/2)\Omega_k\Omega_k$ from being identical. Thus the difference between these signals represent the effects of flow inhomogenities and significant fluctuations of the term $(1/\rho)\nabla^2 p$.

The signals in figure 22 indicate that the strong events seem to be correctly depicted by the present algorithm to determine the intermittency I_t, which behaves like a box-car function. The time-derivative of enstrophy seems also to identify correctly the local maxima/minima.

The PDF of the durations of events, T_e, and that of the timing between these events, T_b, are shown in figure 23. The two distributions are reasonably close to each other. One characteristic feature of the two PDFs is their long tail which is indicative of low-frequency events with low probability of appearance. It is also evident from the two pdfs that the most probable value is $N = 1$. The mean values, however, appear to be $\overline{N_e} = 25$ and $\overline{N_b} = 20$ respectively while the standard deviations are about the same, $\sigma_e \approx \sigma_b \approx 33$. The average value of N_b yields a frequency, non-dimensionalized by inner-wall variables, of $n_b^+ = 0.23$. If this value is compared with the traditional bursting frequency of $n^+ \approx 0.05$ then it can be concluded that the present algorithm identifies strong vortical events which occur more often than the near-wall bursts. The vortical bipolar events identified by our wall-voriticty-flux measurements have a frequency of appearance of about 0.18. In that respect our single-point measurements at $x_2^+ = 12.5$ depict all the vortical structures formed at $x_2^+ = 0$ where vorticity is produced by the non-slip condition at the wall.

The scatter plot of the number of points N_e of a strong event and the number of maxima/minima, N_m, within this event is shown in figure 24 where values are plotted on log-log scales. This type of scatter plot is equivalent to a JPDF. Since the number of max/min N_m cannot be greater than N_e, the line $N_m = N_e$ has also been plotted on the figure. It appears that all the points lie below this line, as they should. The data show large values with rather low-probability events while the largest accumulation

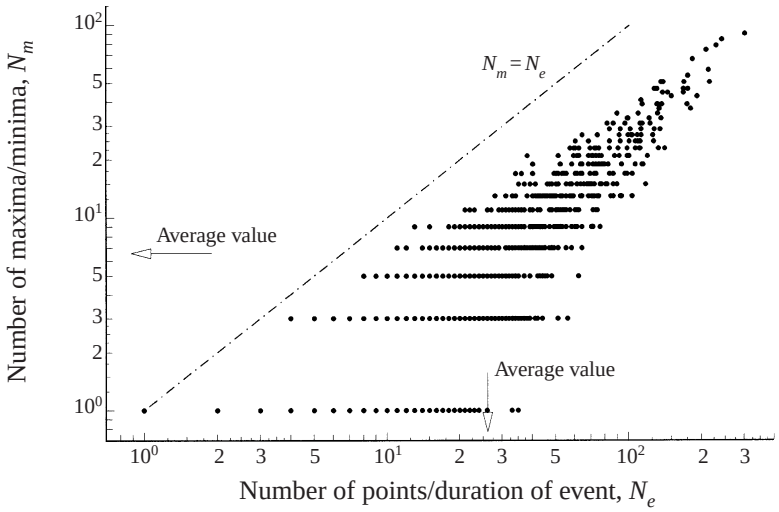

FIGURE 24. Scatter plot of duration of events and corresponding number of maxima/minima within the event.

of points is close to 1 which apparently is the most probable value. The mean value of N_m is $\overline{N_m} = 6.7$ which suggests that the average vorticity-based number of cycles within a strong event is $(1+\overline{N_m})/2 \simeq 4$. This estimate is based on the assumption that each cycle contains one maximum and one minimum. This analysis demonstrates that a sequence of high-vorticity events, possibly a streak of vortices or shear layers can be identified, on average, within a strong vortical structure. Their non-dimensional frequency of appearance expressed in wall viscous units is $n_v^+ = 1.1$. Thus, the present data have shown that there is a bursting mode of events within a strong vortical event which may be interpreted as a streak of vortices. Let us consider how these events are related to the packet of hairpin vortices found in the DNS of Liu & Adrian (1999). The distance between the auto-generated hairpin vortices in the vortex packets of Liu & Adrian appears to be, typically, between 70 and 250 wall viscous units. If the Taylor hypothesis is invoked their frequency of appearance is between $n^+ = 0.08$ and 0.27. These values are close to the present $n_b^+ = 0.23$. In that respect, the strong vortical events identified in the present analysis may be the hairpin vortices found by Liu & Adrian. However, the bursting frequency of vortex streaks inside a strong vortical event, $n_v^+ = 1.1$, is considerably higher than the frequency of hairpins within the packet of Liu & Adrian. In that respect, the substructures within a strong event identified in the present work may be different from the hairpin vortices of Liu & Adrian.

The present results appear to be qualitatively and, to a certain extent, quantitatively independent of the threshold level. However, there is a certain degree of subjectivity involved in the present analysis, as in every conditional analysis of data. This inherent subjectivity is associated with the conditioning statement and hypothesis. There is also considerable subjectivity in the interpretation of the results. Nevertheless, the use of enstrophy as a conditioning function to identify strong vortical events seems quite plausible, since large values of vorticity/enstrophy are always indicative of the presence of strong vortices. Thus, there is considerable confidence that the present techniques can provide some useful information on the structures identified. It is not clear, however, whether these structures are hairpin vortices or some other type of vortices.

7. Conclusions

The experimental data of HA constitute fertile ground for some new analysis and statistical results of wall-bounded turbulence in nominally two-dimensional incompressible boundary layers. The data include time-dependent values of the three components of velocity and vorticity vectors, U_i and Ω_i respectively, and all the components of the velocity-gradient and strain-rate tensors, A_{ij} and S_{ij} respectively. These data were obtained with a spatial resolution of about 7 Kolmogorov viscous length scales in the near-wall region and of about 4 in the outer part of the boundary layer.

In the present analysis, particular emphasis has been given to the time-dependent behaviour of the kinematic shear stress, vorticity, enstrophy, dissipation rate of turbulent kinetic energy, vorticity stretching and several of the matrix invariants of the velocity-gradient tensor, strain-rate tensor and rotation-rate tensor.

A positive correlation coefficient between fluctuations of the longitudinal and normal vorticity components has been found to exist throughout the boundary layer. This value of 0.27 is considerably lower than the -0.4 value of the correlation coefficient between the velocity fluctuations in the same directions.

The invariants have been linked with terms appearing in the transport equations of enstrophy and dissipation rate. Indicative of the existence of extremely high fluctuations is that all r.m.s. values are considerably larger than the mean values of all quantities involving a velocity gradient. All invariants exhibit a very strong intermittent behaviour which is characterized by large amplitude of bursts, which may be of the order of 10 times the r.m.s. values.

The r.m.s. value of the instantaneous production of turbulent kinetic energy is also 10 times higher than the mean production, while the r.m.s. of the dissipation-rate fluctuations is about 1.5 times higher than its mean value. The r.m.s. value of the stretching terms also appears to be about 10 times larger than the spanwise mean stretching. These results clearly suggest that the use of time-average transport equations for turbulent kinetic energy and vorticity can be very misleading in understanding the flow physics and structure. The results also suggest that time-dependent quantities and transport equations should also be considered, where possible, even for design purposes.

The iso-probability contours of the joint probability density function of the invariants of the velocity gradient tensor assume an inverted teardrop shape which is in qualitative agreement with the results of Chaćin *et al.* (1996) which were obtained from the DNS data of Spalart (1988). In that respect the present experimental results confirm the theory and numerical work of Chaćin *et al.*

Patterns with high rates of turbulent kinetic energy dissipation and high enstrophy suggest the existence of strong shear layers in the near-wall region. In many instances, locally high values of the invariants are also associated with peaks in the shear stress as shown in figure 22 and in HA. It appears that the strain dominates the fluctuations of pressure more than enstrophy.

Conditional analysis provided some evidence of the existence of streaks of several vortices during strong vortical activities with an average frequency of appearance four times more than the frequency of hairpin vortices.

The work was initially funded through a grant provided by the National Science Foundation. The first author was supported by a NASA grant NAG3-2163 during the later phases of this work.

Appendix. Velocity gradient computations and numerical schemes

If the origin of a coordinate system is fixed at the centroid of the probe as shown in figure 2(*a*) and subscripts 0, 1, 2 and 3 refer to quantities at the centroid of each of the probes, the centres of first, second and third triple wires respectively, then Taylor expansion of velocity component u at the centroid, neglecting higher order derivative terms, yields

$$u_{1_1} = u_{1_0} + \left(\frac{\partial u_{1_0}}{\partial x_2}\right)_{x_1=x_2=x_3=0} \Delta x_{2_1} + \left(\frac{\partial u_{1_0}}{\partial x_3}\right)_{x_1=x_2=x_3=0} \Delta x_{3_1}, \tag{A 1}$$

$$u_{1_2} = u_{1_0} + \left(\frac{\partial u_{1_0}}{\partial x_2}\right)_{x_1=x_2=x_3=0} \Delta x_{2_2} + \left(\frac{\partial u_{1_0}}{\partial x_3}\right)_{x_1=x_2=x_3=0} \Delta x_{3_2}, \tag{A 2}$$

$$u_{1_3} = u_{1_0} + \left(\frac{\partial u_{1_0}}{\partial x_2}\right)_{x_1=x_2=x_3=0} \Delta x_{2_3} + \left(\frac{\partial u_{1_0}}{\partial x_3}\right)_{x_1=x_2=x_3=0} \Delta x_{3_3}, \tag{A 3}$$

which form the following system of linear equations:

$$\begin{bmatrix} u_{1_1} \\ u_{1_2} \\ u_{1_3} \end{bmatrix} = \begin{bmatrix} 1 & \Delta x_{2_1} & \Delta x_{3_1} \\ 1 & \Delta x_{2_2} & \Delta x_{3_2} \\ 1 & \Delta x_{2_3} & \Delta x_{3_3} \end{bmatrix} \begin{bmatrix} u_{1_0} \\ \dfrac{\partial u_{1_0}}{\partial x_2} \\ \dfrac{\partial u_{1_0}}{\partial x_3} \end{bmatrix}. \tag{A 4}$$

All the elements of the first matrix on the right-hand side can be expressed in terms of 1_0 shown in figure 2(*a*) where Δx_{2i} and $\Delta x_{3i}\,(i = 1, 2, 3)$ are the distances between the centre of the ith triple wire and the centroid of the probe in the x_2- and x_3-directions of the probe coordinate system respectively. The solution of (A 4) yields the longitudinal velocity u_{1_0} and the two spatial derivatives at the centroid of the probe.

Similar equations can be written for the normal component u_{2_0} and its partial derivatives and for the transverse component u_{3_0} and its partial derivatives. Now the streamwise derivatives are obtained by considering the momentum equation and neglecting pressure and viscous forces gradients; the final expressions can be written as

$$\frac{\partial u_{1_0}}{\partial t} + u_{1_0}\frac{\partial u_{1_0}}{\partial x_1} + u_{2_0}\frac{\partial u_{1_0}}{\partial x_2} + u_{3_0}\frac{\partial u_{1_0}}{\partial x_3} = 0. \tag{A 5}$$

Thus

$$\frac{\partial u_{1_0}}{\partial x_1} = -\frac{1}{u_{1_0}}\left[\frac{\partial u_{1_0}}{\partial t} + u_{2_0}\frac{\partial u_{1_0}}{\partial x_2} + u_{3_0}\frac{\partial u_{1_0}}{\partial x_3}\right], \tag{A 6}$$

and similarly for the other gradients of the velocity components in the longitudinal direction:

$$\frac{\partial u_{2_0}}{\partial x_1} = -\frac{1}{u_{1_0}}\left[\frac{\partial u_{2_0}}{\partial t} + u_{2_0}\frac{\partial u_{2_0}}{\partial x_2} + u_{3_0}\frac{\partial u_{2_0}}{\partial x_3}\right], \tag{A 7}$$

$$\frac{\partial u_{3_0}}{\partial x_1} = -\frac{1}{u_{1_0}}\left[\frac{\partial u_{3_0}}{\partial t} + u_{2_0}\frac{\partial u_{3_0}}{\partial x_2} + u_{3_0}\frac{\partial u_{3_0}}{\partial x_3}\right]. \tag{A 8}$$

They have been obtained by considering the momentum equations for the u_2 and u_3 components respectively. These equations are considered as variations of Taylor's hypothesis.

Finally, the temporal derivatives in (A 6)–(A 8) can easily be evaluated by the product of two successive velocity values and sampling frequency f_s which subsequently allows computation of the streamwise derivatives.

Thus the determination of the longitudinal velocity derivatives is not entirely based on the original version of Taylor's hypothesis.

The velocity across each triple sensor is not assumed to be uniform. Thus each wire of one triple-wire probe sees different velocity vectors. However, the velocity along each individual wire is assumed to be uniform. In addition, the velocity gradient between two individual wires is assumed to be the same across the entire probe. Under these assumptions the linear velocity profile is segmented into multiple pieces, nine areas in total.

An iterative scheme was used to improve the solutions obtained with each iteration. The velocity gradients determined by the finite difference described in the previous section were introduced to correct the velocity distribution across the entire probe.

In the orthogonal coordinate system x, y, z of the j-probe ($j = 1, 2, 3$) the components of the velocity vector V_0 at the origin are X_{0j}, Y_{0j}, Z_{0j}. The velocity components at the mid-point of each wire can be estimated as a first-order approximation in a Taylor series expansion. Thus the velocity components at the mid-point $(0, \Delta y, 0)$ of the wire at the $0y$-axis will be

$$X_{0j} + \frac{\partial X_{0j}}{\partial y}\Delta y, \quad Y_{0j} + \frac{\partial Y_{0j}}{\partial y}\Delta y, \quad Z_{0j} + \frac{\partial Z_{0j}}{\partial y}\Delta y.$$

A typical expression for the effective velocity $U_{eff\,ij}$ of the i-wire ($i = 1, 2, 3$) of the j-probe is as follows:

$$U^2_{eff\,ij} = H^2_{ij}(X_{0j} + \frac{\partial X_{0j}}{\partial y}\Delta y)^2 + K^2_{ij}(Y_{0j} + \frac{\partial Y_{0j}}{\partial y}\Delta y)^2 + M^2_{ij}(Z_{0j} + \frac{\partial Z_{0j}}{\partial y}\Delta y)^2. \qquad \text{(A 9)}$$

The coefficients H_{ij}, K_{ij} and M_{ij} are determined through calibrations. Each of the gradients $\partial X_{0j}/\partial y$, $\partial Y_{0j}/\partial y$, $\partial Z_{0j}/\partial y$ can be expressed in terms of the velocity gradients in the coordinates of the centroid by simple transformations.

A system of three equations, one for each of the wires of the triple sensor array, can be solved to provide estimates of the velocity vector (X_{0j}, Y_{0j}, Z_{0j}). The solution procedure is iterative. An initial 'guess' of the velocity components is obtained by assuming that the increments $(\partial X_{0j}/\partial y)\Delta y$, $(\partial Y_{0j}/\partial y)\Delta y$, $(\partial Z_{0j}/\partial y)\Delta y$ are initially zero. Then the velocity vectors at the origin of each of the triple-wire probes can be obtained and subsequently the velocity gradients can be computed by the finite difference scheme described previously. This leads to the first estimates of all partial velocity gradients which can be introduced into (A 9) and a second estimate of velocity vectors and velocity gradients can be obtained. The iteration stops when the solutions converge. Usually, a small number of iterations is needed. The results at $x_2^+ = 12.5$ indicate that about 82% of the number of samples processed converged after two iterations only. The data also have shown that the number of iterations needed never exceeded 10 for any of the samples considered.

REFERENCES

ANDREOPOULOS, J. 1983*a* Improvements of the performance of triple hot wire probes. *Rev. Sci. Instrum.* **54**, 733–740.

ANDREOPOULOS, J. 1983*b* Statistical errors associated with turbulence intensity and probe geometry in hot-wire anemometry. *J. Phys.* E *Sci. Instrum.* **16**, 1264–1271.

Andreopoulos, J. & Agui, J. H. 1996 Wall-vorticity flux dynamics in a two-dimensional turbulent boundary layer. *J. Fluid Mech.* **309**, 45–84.

Andreopoulos, Y., Agui, J. H. & Briassulis, G. 2000 Shock wave turbulence interactions. *Ann. Rev. Fluid Mech.* **32**, 309–345.

Andreopoulos, J., Durst, F., Zarić, Z. & Jovanovic, J. 1984 Influence of Reynolds number on characteristics of turbulent wall boundary layers. *Exps. Fluids* **2**, 7–16.

Andreopoulos, J. & Wood, D. 1982 The response of a turbulent boundary layer to short length of roughness. *J. Fluid Mech.* **118**, 143–164.

Antonia, R. H., Zhu, Y. & Kim, J. 1993 On the measurement of lateral velocity derivatives in turbulent flows. *Exps. Fluids* **15**, 65–69.

Balint, J., Wallace, J. M. & Vukoslavcevic, P. 1991 The velocity and vorticity vector fields of a turbulent boundary layer. Part 2. Statistical properties. *J. Fluid Mech.* **228**, 53–86.

Blackburn, H. M., Mansour, N. N. & Cantwell, B. J. 1996 Topology of fine-scale motions on turbulent channel flow. *J. Fluid Mech.* **310**, 269–392.

Blackwelder, R. F. & Haritonidis, J. H. 1983 Scaling of the bursting frequency in turbulent boundary layers. *J. Fluid Mech.* **132**, 87–103.

Bradshaw, P., Ferris, D. H. & Atwell, N. P. 1967 Calculation of boundary layer development using the turbulent energy equation. *J. Fluid Mech.* **28**, 593–611.

Bradshaw, P. & Huang, G. P. 1995 The law of the wall in turbulent flow. *Proc. R. Soc. Lond.* A **451**, 165–188.

Briassulis, G., Agui, J. & Andreopoulos, Y. 2001 The structure of weakly compressible grid turbulence. *J. Fluid Mech.* **432**, 219–283.

Cantwell, B. J. 1993 On the behavior of velocity gradient tensor invariants in direct numerical simulations of turbulence. *Phys. Fluids* A **5**, 2008–2013.

Chaćin, J. M., Cantwell, B. J. & Kline, S. J. 1996 Study of turbulent boundary layer structure using invariants of velocity gradient tensor. *Expl Thermal Fluid Sci.* **13**, 308–317.

Chevray, R. & Tutu, N. K. 1978 Intermittency and preferential transport of heat in a round jet. *J. Fluid Mech.* **88**, 133–160.

Chong, M. S. Perry, A. E. & Cantwell, B. J. 1990 A general classification of three-dimensional flow fields. *Phys. Fluids* A **2**, 765–777.

Gupta, A. K. & Kaplan, R. E. 1972 Statistical characteristics of Reynolds stress in a turbulent boundary layer. *Phys. Fluids* **15**, 981–985.

Honkan, A. 1994 An experimental study of the vortical structure of turbulent flows. PhD Thesis, City University of New York.

Honkan, A. & Andreopoulos, J. 1993 Direct calibration mapping and data analysis in triple hot-wire anemometry. In *Thermal Anemometry* (ed. D. Stock, A. Serif & A. J. Smits). ASME. FED vol. 1, p. 67.

Honkan, A. & Andreopoulos, Y. 1997*a* Vorticity, strain-rate and dissipation characteristics in the near-wall region of turbulent boundary layers. *J. Fluid Mech.* **350**, 29–96.

Honkan, A. & Andreopoulos, Y. 1997*b* Instantaneous three dimensional vorticity measurements in vortical flow over a delta wing. *AIAA J.* **35**, 1612–1620.

Kasagi, N., Sumitani, Y., Suzuki, Y. & Iida, O. 1995 Kinematics of the quasi-coherent vortical structure in near-wall turbulence. *Intl J. Heat Fluid Flow* **16**, 2–10.

Kim, J., Moin, P. & Moser, R. 1987 Turbulence statistics in fully developed channel flow at low Reynolds number. *J. Fluid Mech.* **177**, 133–166.

Klebanoff, P. S. 1954 Characteristics of turbulence in a boundary layer with zero pressure gradient. *NACA TN* 3178.

Klewicki, J. C. & Falco, R. E. 1990 On accurately measuring statistics associated with small-scale structure in turbulent boundary layers using hot-wire probes. *J. Fluid Mech.* **219**, 119–142.

Kolmogorov, A. A. 1941 The local structure of turbulence in incompressible viscous fluid for very large Reynolds numbers. *C. R. Akad. Sci. SSSR* **30**, 301–306.

Lemonis, G. C. 1995 An experimental study of the vector fields of velocity and vorticity in turbulent flows. Doctoral Thesis, Swiss Federal Institute of Technology, Institute of Hydromechanics and Water Resources.

Liu, Z. & Adrian, R. J. 1999 Evidence of hairpin packet structure in DNS channel flow. *Bull. Am. Phys. Soc.* **44**, 33.

Mansour, N. N., Kim, J. & Moin, P. 1988 Reynolds-stress and dissipation-rate budgets in a turbulent channel flow. *J. Fluid Mech.* **194**, 15–44.

Meinhart, C. D. & Adrian, R. J. 1995 On the existence of uniform momentum zones in a turbulent boundary layer. *Phys. Fluids* **7**, 694–696.

Moser, R., Kim, J. & Mansour, N. N. 1999 Direct numerical simulation of turbulent channel flow up to $Re_\tau = 590$. *Phys. Fluids* **11**, 943–944.

Moser, R. & Rogers, M. 1993 Three dimensional evolution of a plane mixing layer: Pairing and transition to turbulence. *J. Fluid Mech.* **247**, 275–301.

Ong, L. & Wallace, J. M. 1998 Joint probability density analysis of the structure and dynamics of vorticity field of a turbulent boundary layer. *J. Fluid Mech.* **367**, 291–328.

Perry, A. E. & Chong, M. S. 1982 On the mechanism of wall turbulence. *J. Fluid Mech.* **119**, 173–217.

Perry, A. E. & Chong, M. S. 1987 A description of eddying motions and flow patterns using critical point concepts. *Ann. Rev. Fluid Mech.* **19**, 125–155.

Perry, A. E., Henbest, S. M. & Chong, M. S. 1986 A theoretical and experimental study of wall turbulence. *J. Fluid Mech.* **165**, 163–199.

Robinson, S. K. 1991 Coherent motions in the turbulent boundary layer. *Ann. Rev. Fluid Mech.* **23**, 601–639.

Smith, C. R. & Walker, J. D. A. 1995 Turbulent wall-layer vortices. In *Fluid Vortices* (ed. S. I. Green). Kluver.

Soria, J., Sondergaard, R., Cantwell, B. J. & Perry A. E. 1994 A study of the fine-scale motions of incompressible time-developing mixing layers. *Phys. Fluids* **6**, 871–883.

Spalart, P. R. 1988 Direct simulation of a turbulent boundary layer up to $R_\theta = 1410$. *J. Fluid Mech.* **187**, 61–98.

Spalding, D. B. 1961 A single formula for the law of the wall. *Trans. ASME* E: *J. Appl. Mech.* **28**, 455–458.

Theodoresen, T. 1952 Mechanism of turbulence. *Proc. 2nd Midwestern Conf. on Fluid Mechanics, Ohio State University, Columbus, Ohio*.

Townsend, A. A. 1951 On the fine-scale structure of turbulence. *Proc. R. Soc. Lond.* A **208**, 534–542.

Townsend, A. A. 1976 *The Structure of Turbulent Shear Flow*. Cambridge University Press.

Tsinober, A., Kit, E. & Dracos, T. 1992 Experimental investigation of the field of velocity gradients in turbulent flows. *J. Fluid Mech.* **242**, 169–192.

Tutu, N. K. & Chevray, R. 1975 Cross-wire anemometry in high intensity turbulence. *J. Fluid Mech.* **71**, 785–800.

Vukoslavcevic, P., Wallace, J. M. & Balint, J. 1991 The velocity and vorticity vector fields of a turbulent boundary layer. Part 1. Simultaneous measurement by hot-wire anemometry. *J. Fluid Mech.* **228**, 25–51.

Wallace, J. M. & Foss, J. 1995 The measurement of vorticity in turbulent flows. *Ann. Rev. Fluid Mech.* **27**, 469–514.

Wyngaard, J. C. 1969 Spatial resolution of the vorticity meter and other hot-wire arrays. *J. Phys.* E: *Sci. Instrum.* **2**, 983–987.

Wood, D. H. & Bradshaw, P. 1982 A turbulent mixing layer constrained by solid surface. Part 1. Measurements before reaching the surface. *J. Fluid Mech.* **122**, 57–89.